Astronomy
&
Astrophysics

The jet paths of radio active galactic nuclei and their cluster weather

E. Vardoulaki[1,2,*] , V. Backöfer[2] , A. Finoguenov[3] , F. Vazza[4,5,6] , J. Comparat[7] , G. Gozaliasl[3,8] ,
I. H. Whittam[9] , C. L. Hale[9] , J. R. Weaver[10,11,12] , A. M. Koekemoer[13] , J. D. Collier[14,15,16] , B. Frank[14,17,18] ,
I. Heywood[9,19] , S. Sekhar[14,21] , A. R. Taylor[20,14,16] , S. Pinjarkar[22] , M. J. Hardcastle[22] , T. Shimwell[23,24] , M. Hoeft[2] ,
S. V. White[30] , F. An[25,26] , F. Tabatabaei[27,28,29] , Z. Randriamanakoto[30,31] , and M. D. Filipovic[15]

(Affiliations can be found after the references)

ABSTRACT

We studied bent radio sources within X-ray galaxy groups in the COSMOS and XMM-LSS fields. The radio data were obtained from the MeerKAT International GHz Tiered Extragalactic Explorations data release 1 (MIGHTEE-DR1) at 1.2–1.3 GHz, with angular resolutions of 8.9″ and 5″, and median noise levels of $rms_{med} \sim= 3.5$ and $5.5\,\mu Jy/beam$. Bent radio active galactic nuclei (AGN) were identified through visual inspection. Our analysis included 19 bent radio AGN in the COSMOS field and 17 in the XMM-LSS field that lie within X-ray galaxy groups ($2 \times 10^{13} \lesssim M_{200c}/M_\odot \leq 3 \times 10^{14}$). We investigated the relationship between their bending angle (BA) – the angle formed by the jets or lobes of two-sided radio sources associated with AGN – and the properties of their host galaxies and large-scale environment probed by the X-ray galaxy groups. Our key findings are: (a) In the XMM-LSS field, we observed a strong correlation between the linear projected size of the bent AGN, the group halo mass, and the projected distance from the group centre. This trend, consistent with previous studies, was not detected in the COSMOS sample. (b) The BA is a function of environmental density, with the type of medium playing a significant role. Additionally, at $z \leq 0.5$ we found a higher number of bent sources (BA $\leq 160°$) compared to higher redshifts ($z \sim 1$), by a factor of >1.5. This trend aligns with magneto-hydrodynamic simulations, which suggest that denser environments and longer interaction times at lower redshifts contribute to this effect. A comparison with the literature suggests that jet bending in galaxy groups within the redshift range $0.1 < z < 1.2$ is primarily driven by ram pressure exerted on the jets, which occurs during quiescent phases of AGN activity. This study underscores the role of environmental interactions in shaping the morphology of radio AGN within galaxy groups, providing insights into the interplay between large-scale structure and AGN physics.

Key words. galaxies: abundances – galaxies: active – galaxies: clusters: intracluster medium – galaxies: groups: general – galaxies: jets

1. Introduction

Active galactic nuclei (AGN) in the radio come in many shapes and sizes. These puzzling astrophysical phenomena are related to large-scale structure and galaxy growth and evolution, while their shapes often reveal hints about their interaction with the large-scale environment. (e.g. Prestage & Peacock 1988; Smolčić et al. 2017a; Croston et al. 2019). Their jets, ejected in opposite directions from their supermassive black holes, interact with their surrounding environment, which can cause the jets to deviate from an expected straight morphology. New radio surveys add to the complexity of radio structures (e.g. Hurley-Walker et al. 2017; White et al. 2020a,b; Sejake et al. 2023), as higher resolutions and sensitivities reveal detailed jet structures as well as faint emission that previously eluded observation (e.g. Delhaize et al. 2021; Mahatma et al. 2023). Both radio AGN and star-forming galaxies (SFGs) emit non-thermal synchrotron radiation in the radio (e.g. Miley 1980; Condon 1992; Padovani et al. 2017; Klein et al. 2018), albeit as a result of different physical processes. Nevertheless, the radio signatures of AGN and SFGs can often get tangled up and become indistinguishable without the use of ancillary multi-wavelength observations. Separating the radio AGN and SFG populations in radio continuum surveys is a difficult task as surveys probe deeper populations of the radio sky (e.g. White et al. 2015, 2017; Smolčić et al. 2017a; Gürkan et al. 2018; Vardoulaki et al. 2019, 2021a; Mingo et al. 2019; Whittam et al. 2022). As this study

investigates the jet distortion of extended radio AGN, and their deviation from a straight radio structure, we rely on the distinct jet features to select our samples from visual inspection.

Jet distortion is a complex phenomenon, as jets are observed from parsec to megaparsec scales and evolve over millions of years (Turner & Shabala 2015). Studies suggest jet distortion has a complex explanation and several causes. These include the jets' movement through the intergalactic medium (IGM; e.g. Begelman et al. 1979; Owen & Rudnick 1976; Garon et al. 2019), buoyancy forces (e.g. Sakelliou et al. 1996; Smolčić et al. 2007), precession of jets (e.g. Taylor et al. 1990; Caproni et al. 2017), gravitational interaction of companion galaxies (e.g. Perley et al. 1979; Begelman et al. 1984), or jets passing through an area with significant pressure gradients (e.g. Best et al. 1997).

Past studies that have investigated jet bending in relation to the large-scale environment have mainly employed surveys like FIRST (beam size: 5″, rms: 150 μJy/beam, Becker et al. 1995) or LoTSS (beam size: 6″, rms: 83 μJy/beam, Shimwell et al. 2019, 2022), which cover large areas at the expense of sensitivity, resulting in samples consisting of millions of radio galaxies. Identifying bent radio AGN in large surveys and studying them in relation to their large-scale environment is not a trivial task. A plethora of good-quality multi-wavelength data is required for such studies. Garon et al. (2019) studied the bending angle (BA) of 4304 radio galaxies, selected from FIRST, in optically selected galaxy clusters with masses[1] ranging from $M_{500} =$

---

* Corresponding author; elenivard@gmail.com

[1] $M_{500} =$ is the mass of a cluster or group at a virial radius of 500 times the critical density of the Universe.

$5 \times 10^{14}\,\mathrm{M}_\odot$ to $3 \times 10^{15}\,\mathrm{M}_\odot$. They find that, statistically, the more the sources are bent, the closer they are to their cluster centre. Additionally, sources are more bent in more massive clusters, which is related to higher intracluster medium (ICM) pressures and galaxies moving through the ICM with higher velocities, which promotes jet bending due to ram pressure. Bent sources not located in known clusters are found in statistically overdense regions. Mingo et al. (2019) find that the 459 bent radio galaxies obtained from the LoTSS surveys have a significantly higher rate of cluster association than their total sample of 5805 extended radio sources. While Garon et al. (2019) and Mingo et al. (2019) are limited to cluster redshifts up to 0.8 and 0.4, respectively, Golden-Marx et al. (2021) find 36 bent radio sources, selected from FIRST, in clusters up to redshift 2.2. They find that more bent sources tend to reside in richer clusters, which further supports that bent sources are found in the dense medium of massive clusters, even at higher redshifts. Additionally, in the LoTSS DR2 sample, Golden-Marx et al. (2023) find that narrower sources lie inside clusters, which implies environmental differences in the populations of bent radio AGN. Simulations of galaxies in cluster environments also give insights into the relationship between jet morphology and cluster environments. In particular, Mguda et al. (2015) investigated the likelihood of finding radio galaxies bent due to ram pressure in clusters of galaxies. They find that with increasing halo mass, the number of galaxies bent due to ram pressures increases, but since more massive clusters are rarer than less massive clusters, approximately the same number of galaxies bent due to ram pressure are found at halo masses above and below $\mathrm{M}_{\mathrm{halo}} = 3 \times 10^{14}\,\mathrm{M}_\odot$. Mguda et al. (2015) find that bent radio sources are found out to distances of 1.5 Mpc for clusters with halo masses of $\mathrm{M}_{\mathrm{halo}} \geq 10^{15}\,\mathrm{M}_\odot$ from their cluster centre, whereas the bent sources in clusters with halo masses of $10^{13}\,\mathrm{M}_\odot \leq \mathrm{M}_{\mathrm{halo}} \leq 10^{14}\,\mathrm{M}_\odot$ are most likely found within 400 kpc of their cluster centre.

This study investigates a different parameter space, extending the halo mass range of galaxy groups or clusters to lower halo masses ($4 \times 10^{12}\,\mathrm{M}_\odot < \mathrm{M}_{\mathrm{200c}} < 3 \times 10^{14}\,\mathrm{M}_\odot$). We choose two extragalactic fields, COSMOS and XMM-LSS, to study the radio population and produce samples of extended radio galaxies. This contrasts with studies like those of Garon et al. (2019) and Mingo et al. (2019), who rely on citizen science projects like the Radio Galaxy Zoo or automated source detection pipelines to obtain large samples. Choosing to study well-known fields allows us to utilise deep radio surveys like the 3 GHz VLA-COSMOS project (Smolčić et al. 2017b) with a sensitivity of 2.3 μJy/beam and the ~1.2–1.3 GHz MeerKAT International GHz Tiered Extragalactic Explorations (MIGHTEE) survey (Jarvis et al. 2016; Heywood et al. 2022; Hale et al. 2025) at roughly 2 μJy/beam. Furthermore, legacy fields like COSMOS are well studied across the electromagnetic spectrum, which allows for comprehensive source characterisation and direct comparisons to past and future studies. One such study is from Vardoulaki et al. (2021a,b), who previously investigated the population of bent radio sources in COSMOS with 3 GHz VLA observations with sub-arcsecond resolution (0″.75). Each source was classified based on the scheme by Fanaroff & Riley (1974) as being an edge-darkened FRI-type source, an edge-brightened FRII-type source, or a hybrid FRI/FRII, where one side is edge-darkened and the other edge-brightened. They investigated the relations of bent radio sources to their host properties, FR-type, the large-scale environment probed by the density fields and cosmic-web probes in COSMOS (Scoville et al. 2013; Darvish Sarvestani 2015; Darvish et al. 2017), and the group environments obtained from X-ray galaxy groups in

COSMOS with halo masses $\mathrm{M}_{500} = 5 \times 10^{12}\,\mathrm{M}_\odot$ to $2 \times 10^{14}\,\mathrm{M}_\odot$ (Gozaliasl et al. 2019). They also compared the BA to magneto-hydrodynamical simulations of radio sources in clusters from Vazza et al. (2021). While Vardoulaki et al. (2021b) found no strong correlations between jet bending and the large-scale environment, FR-type, or host properties, they found indications that FRI type radio sources are found in filaments. Differences to other studies of bent radio sources (e.g. Garon et al. 2019) are attributed to either a low sample size or the different parameter space of the studies. Comparisons of Vardoulaki et al. (2021b) to the simulations of Vazza et al. (2021) indicate that sources are more bent at lower redshifts, which may be attributed to a denser ambient medium at lower redshifts.

In this paper, we further investigate the jet bending of extended radio AGN in the COSMOS and XMM-LSS fields with the first data release of the MIGHTEE radio survey (Hale et al. 2025). This study is complementary to past studies and expands the investigation of the BA of radio AGN to higher redshift (up to $z \sim 3.5$) and lower halo mass ($\sim 10^{13-14.5}\,M_\odot$). In Sect. 2, we present the sample creation process and all relevant multi-wavelength observations utilised in this work. The methods are given in Sect. 3. The analysis and discussion of our data are presented in Sects. 4, 5, and 6. Section 5 discusses the results in the context of past and current literature, focusing on sources in galaxy group environments. In Sect. 6, we estimate the expected temperature of the intergalactic medium required to explain the BA and peculiar velocity of the radio host. We present our conclusions in Sect. 7. Throughout this work, we adopt a flat ΛCDM cosmology, using $\mathrm{H}_0 = 70\,\mathrm{km\,s}^{-1}\,\mathrm{Mpc}^{-1}$, $\Omega_m = 0.3$, and $\Omega_\Lambda = 0.7$.

2. Sample selection

2.1. MIGHTEE

The MeerKAT International Gigahertz Tiered Extragalactic Explorations (MIGHTEE, Jarvis et al. 2016; Heywood et al. 2022; Hale et al. 2025) is a galaxy evolution survey currently underway, conducted by the MeerKAT radio telescope in South Africa (Jonas & Team 2016). With ~1000 hours of observing time, the survey aims to image 20 deg^2 over four extragalactic fields: The European Large Area *ISO* Survey South 1 (ELAIS-S1), the Extended Chandra Deep Field South (E-CDFS), and the fields that are the focus of this work: XMM-LSS and COSMOS. The survey aims for a depth of ~2 μJy/beam at ~1.2–1.3 GHz[2]. This work uses the data release DR1 (henceforth MIGHTEE-DR1 Hale et al. 2025), providing a sky coverage of ~14.4 deg^2 in XMM-LSS and ~4.2 deg^2 in COSMOS.

Both radio mosaics from the MIGHTEE-DR1 have been primary beam-corrected and were imaged with two different visibility weighting schemes, resulting in two versions of radio maps for each field. The first version has a lower resolution than the second but is more sensitive. The second version down-weights the short baselines resulting in a higher resolution but decreases the sensitivity of the data. The resulting radio maps have a resolution of 8.9″ with a measured sensitivity (median rms) of ~3.5 μJy/beam, and a resolution of ~5″ with a sensitivity of ~6 μJy/beam. In detail, the median rms for the XMM-LSS field is 5.1 (3.2) μJy/beam for the 5″ (8.9″) mosaic, while for the COSMOS mosaic is 5.6 (3.5) μJy/beam. For the rest of this study, we distinguish the different versions by their resolutions. For more information on data reduction, we refer the reader to

---

[2] We note that the frequency varies across the mosaics.

the related publications (Jarvis et al. 2016; Heywood et al. 2022; Hale et al. 2025).

We identified 306 extended radio structures in XMM-LSS, and 254 extended radio structures in COSMOS after visual inspection of the MIGHTEE-DR1 mosaics. Although automated radio source identification methods have become sufficient in identifying simple radio structures (e.g. PyBDSF Mohan & Rafferty 2015; Polsterer et al. 2019), even the more sophisticated automatic algorithms fail in identifying complex radio structures (e.g. Vardoulaki et al. 2021a; Boyce et al. 2023). Additionally, although automatic algorithms such as PINK (Galvin et al. 2020) are very useful in identifying radio structures, matching to the host galaxy and classifying sources, they need a good training sample that depend on resolution and sensitivity (e.g. Vardoulaki et al. 2021a). Since our project depends on the good identification of radio structures in the MIGHTEE mosaics and of their associated hosts, and since there was no extended source catalogue for MIGHTEE-DR1 at the beginning of the project and during the time the analysis took place, we chose the traditional way of visual inspection.

Below, we describe the process of cleaning up these samples to include only two-sided radio AGN, for which we could securely measure their BA (see Sect. 3.3). For this reason, we used a large variety of multi-wavelength data. To the best of our ability, these samples of bent radio AGN include all sources for which we could securely measure the BA. The final samples, relevant to this analysis, contain extended radio AGN within the X-ray galaxy groups in the COSMOS and XMM-LSS fields (Table 2). The radio properties of the final sample are presented in the appendix (Tables B.1 and B.2; available via CDS).

2.2. Multi-wavelength data

2.2.1. VLA-COSMOS

For the COSMOS field, we utilise observations from the Very Large Array (VLA), which provide both excellent resolution and sensitivity, to improve the source characterisation in the COSMOS sample. The VLA-COSMOS 1.4 GHz Large Project (Schinnerer et al. 2007), was performed using the VLA and consists of 23 pointings covering the $2\,deg^2$ of the COSMOS field with a total observing time of 275 hours. The mean sensitivity reaches $10.5\,\mu Jy/beam$ ($15\,\mu Jy/beam$) in the central deg^2 ($2\,deg^2$), which is 2–3 times worse than the MIGHTEE-DR1, but the VLA data have much higher angular resolution than MIGHTEE-DR1. The beam size of the VLA mosaic is $1.4'' \times 1.5''$.

The VLA-COSMOS 3 GHz Large Project (Smolčić et al. 2017b) covers a sky area of $2.6\,deg^2$ with 64 pointings, fully covering the central $2\,deg^2$ of the COSMOS field, and expanding the area to $2.6\,deg^2$. It reaches a median rms of $2.3\,\mu Jy/beam$ at the centre of the field and a sub-arcsecond resolution of $0.75''$, allowing us to study the sub-structures in high resolution and helping us to disentangle sources.

2.2.2. GMRT 610 MHz

In rare cases, we used the 610 MHz GMRT observations for the XMM-LSS sample to get a better understanding of the sources morphologies. The GMRT 610 MHz radio continuum survey (Smolčić et al. 2018) was conducted by the Giant Metrewave Radio Telescope at 50 cm wavelength, covering $25\,deg^2$ over the XXL Northern field (XXL-North). The survey combined previous observations done with the GMRT at 610 MHz,

covering an area of $12.66\,deg^2$ within XXL-North, which also includes XMM-LSS (Tasse et al. 2007). For the area that encloses XMM-LSS, Smolčić et al. (2018) reports a median rms of $200\,\mu Jy/beam$, improving from the reported rms of $300\,\mu Jy/beam$ from Tasse et al. (2007). The synthesised beam size of the final mosaic is $6.5'' \times 6.5''$.

2.2.3. VLASS

Because it was not always possible to determine the core region of the radio sources from the MIGHTEE data alone, we also used high frequency, high resolution data from the 3 GHz Very Large Array Sky Survey (Lacy et al. 2020, VLASS), if necessary. VLASS is an all-sky radio survey that covers the entire sky observable by VLA north of a declination of –40 deg, covering completely both the XMM-LSS and COSMOS fields. The survey aims to cover an area of $33\,885\,deg^2$ with an angular resolution of $2.''5$ down to noise levels of $70\,\mu Jy/beam$ by 2024. For this study, we use the Epoch 1 Quick Look images (Gordon et al. 2020) provided by the Canadian Initiative for Radio Astronomy Data Analysis (CIRADA[3]), offering radio cutouts with an rms $\sim 0.12\,mJy/beam$ (see Table 1).

2.2.4. HSC-SSP

The Hyper Suprime-Cam Subaru Strategic Program (Aihara et al. 2018, HSC-SSP) provides deep optical data for both COSMOS and XMM-LSS with multi-band (g, r, i, z, y plus four narrow-band filters) imaging. The survey was carried out by the wide-field camera HSC on the 8.2 m Subaru telescope. The data is three-layered (wide, deep, ultradeep), covering an area and depth of about $1200\,deg^2$ ($r \sim 26$), $27\,deg^2$ ($r \sim 27$) and $3.5\,deg^2$ ($r \sim 28$), respectively. For this work, we utilise the optical wide i-band images from the third public data release (Aihara et al. 2022, PDR3), as well as the photometric redshift catalogue computed from their data from the second public data release (Nishizawa et al. 2020, PDR2) to look for host positions and photometric redshifts for the XMM-LSS sample.

2.2.5. COSMOS2020

COSMOS2020 (Weaver et al. 2022) is the latest release of the photometric catalogue for the Cosmic Evolution Survey, building on the previous releases by Capak et al. (2007), Ilbert et al. (2008, 2013), Muzzin et al. (2013) and Laigle et al. (2016). The catalogue contains source detection with multi-wavelength photometry for over 1.7 million sources, providing two independent photometric redshift estimates (LePhare: Arnouts et al. 2002; Ilbert et al. 2006, EAZY: Brammer et al. 2008) for all sources. For $i < 21$ objects, the photometric redshift accuracy is better than 1%, while the fainter objects $25 < i < 27$ reach a precision level of 5%. Where available, we used the COSMOS2020 data to determine the host position and photometric redshifts (Weaver et al. 2022) for the COSMOS sample in this work.

2.2.6. WISE

WISE $3.4\,\mu m$ images (Wright et al. 2010) were first used to assign preliminary host positions for the XMM-LSS sample before using the higher resolved and deeper HSC-SSP images, and for the host positions for COSMOS sources positioned at the edge of the MIGHTEE-DR1 mosaic, where there is no coverage from COSMOS2020. Since WISE W1 is close to mid-IR, it

---

[3] http://cutouts.cirada.ca/

Table 1. Radio data used in this work.

Survey	Central Frequency	Sensitivity	Beam Size	Field	Reference
MIGHTEE-DR1	1.2–1.3 GHz	3.5 μJy/beam	8.9″ × 8.9″	COSMOS	Hale et al. (2025)
MIGHTEE-DR1	1.2–1.3 GHz	3.2 μJy/beam	8.9″ × 8.9″	XMM-LSS	Hale et al. (2025)
MIGHTEE-DR1	1.2–1.3 GHz	5.6 μJy/beam	5.2″ × 5.2″	COSMOS	Hale et al. (2025)
MIGHTEE-DR1	1.2–1.3 GHz	5.1 μJy/beam	5″ × 5″	XMM-LSS	Hale et al. (2025)
VLASS Epoch 1	3 GHz	0.12 mJy/beam	2.5″ × 2.5″	XMM-LSS&COSMOS	Lacy et al. (2020)
3 GHz VLA	3 GHz	2.3 μJy/beam	0.75″ × 0.75″	COSMOS	Smolčić et al. (2017b)
1.4 GHz VLA	1.4 GHz	15 μJy/beam	1.4″ × 1.5″	COSMOS	Schinnerer et al. (2010)
GMRT 610 MHz	610 MHz	200 μJy/beam	6.5″ × 6.5″	XMM-LSS	Smolčić et al. (2018)

samples a different galaxy population than HSC-SSP (mentioned below), which both use versions of *grizy* passbands. Therefore, WISE images are still useful for finding fainter galaxies that cannot be observed in the optical passbands of HSC-SSP.

2.3. Fields

2.3.1. XMM-LSS

For the 306 identified extended sources in XMM-LSS, overlays from both MIGHTEE resolutions were produced with background images of WISE W1 and HSC-SSP wide *i*-band to look for the host positions, using the VLASS and GMRT radio data when necessary (see Sect. 2.2). For 282 of the 306 sources in XMM-LSS, we could assign a host position (92%).

2.3.2. COSMOS

For COSMOS, we also used the 1.4 GHz and 3 GHz VLA data, when available, to aid in the search for the correct host. The sample of extended radio sources from the 3 GHz VLA data in COSMOS from Vardoulaki et al. (2021a) was used as a reference for the COSMOS sample in this work. We note that MeerKAT is sensitive to extended diffuse emission, due to the short baselines in its core, while the VLA resolves out some extended emission, causing extended sources to be missed (often only the compact parts are detected). Because of the difference in sensitivity and coverage of the MIGHTEE COSMOS data, visual inspection of the MIGHTEE data still yielded many extended radio sources that were previously not at the 3 GHz data. We found 20 extended sources with jets from diffuse emission in MIGHTEE that are either not detected by the VLA or are at the noise level of the 3 GHz survey. In some cases, the extended sources found in MIGHTEE could be seen in the 3 GHz data by going below the 3σ noise level. This was a useful tool for the source characterisation in the COSMOS sample, as the 3 GHz data at 1σ showed peaked emission along the jets and hotspots in the lobes, which is hidden in the noise. On the other hand, out of the 108 extended radio sources with a BA presented in Vardoulaki et al. (2021a), 48 (44%) are not found in our sample from visual inspection of the MIGHTEE data. This is because the resolution of the MIGHTEE-DR1 data is insufficient to resolve the jet structures and substructures of radio sources $\lesssim20''$. At redshift 1, the 5″ beam size of MIGHTEE corresponds to ≈40 kpc, while the 0.″75 beam of 3 GHz VLA resolves ≈6 kpc. For a redshift of 2, these beam sizes correspond to ≈42 kpc and ≈6.3 kpc, respectively.

By using the multi-wavelength data (optical, infrared and radio), as well as visual inspection, we were able to assign a host position for 193 out of 254 radio sources in the COSMOS field (76%). In COSMOS, many extended radio structures turned out to be blended point-like sources when analysed with multi-wavelength data, thus resulting in a lower host association percentage when compared to the XMM-LSS sample.

2.4. Redshifts

For both the XMM-LSS and COSMOS samples, we use spectroscopic redshifts provided by the HSC-SSP PDR3 data access website[4], which offers a collection of public spectroscopic redshift surveys. The spectroscopic redshifts surveys are from PRIMUS (Coil et al. 2011; Cool et al. 2013), VIPERS (Garilli et al. 2014), SDSS (Alam et al. 2015; Ahumada et al. 2020), UDSz (Bradshaw et al. 2013; McLure et al. 2013), GAMA (Liske et al. 2015), 6dFGRS (Jones et al. 2009), VVDS (Le Fèvre et al. 2013), VANDELS (Pentericci et al. 2018), DEIMOS-10k (Hasinger et al. 2018), 2dFGRS (Colless et al. 2003), zCOSMOS (Lilly et al. 2009), 3D-HST (Skelton et al. 2014; Momcheva et al. 2016), FMOS (Silverman et al. 2015), WiggleZ (Drinkwater et al. 2010), DEEP2 (Newman et al. 2013), DEEP3 (Cooper et al. 2011), C3R3 (Masters et al. 2017, 2019) and LEGA-C (Straatman et al. 2018). In addition, we use the spectroscopic redshifts from the IMACS survey (Kelson et al. 2014) in COSMOS. We also utilise the near position search from the NASA/IPAC Extragalactic Database[5] (NED) for a handful of sources to obtain a spectroscopic redshift value. Spectroscopic redshifts are available for 47% of the XMM-LSS sample (89 out of 189 sources) and for 34% of the COSMOS sample (39 out of 116 sources).

For photometric redshifts in XMM-LSS, we use the Mizuki photometric redshift wide catalogue from the HSC-SSP second public data release Nishizawa et al. (2020), which uses template fitting with Bayesian priors on physical properties of galaxies to compute the most probable redshift, and which completely covers the area of XMM-LSS in the MIGHTEE-DR1. Only objects that have been observed with at least three bands are included in the catalogue and we only consider redshifts that have a reduced $\chi^2_\nu < 5$ from the best-fit model (Nishizawa et al. 2020). We have investigated the photometric redshift catalogue of Hatfield et al. (2022) and compared to the Mizuki photometric redshifts. We find that the redshifts agree within the errors in most cases (>95%). Inside galaxy groups, which is important for this study, there is no difference.

For COSMOS, we use the photometric redshifts from COSMOS2020 computed with LePhare (Weaver et al. 2022), if secure spectroscopic redshift were not available. We note that the quality of the photometric redshifts outside the region that is

---

[4] https://hsc-release.mtk.nao.ac.jp/doc/index.php/catalog-of-spectroscopic-redshifts__pdr3

[5] https://ned.ipac.caltech.edu/

Table 2. Sample size overview.

Sample	XMM-LSS	COSMOS
From visual inspection	306	254
With host	282	193
With bending angle	217	142
With redshift	189	116
Within X-ray coverage	183	76
Inside X-ray Galaxy Groups	17	19

Notes. The succeeding line is always a sub-sample of the preceding line. The last line presents the final sample used in this analysis.

covered by UltraVISTA is worse compared to the inner region of the field. Because the sources from outside the UltraVISTA region are missing the $YJHK_s$ bands and are only selected from i and z bands, we expect to lose redshift accuracy as the optical rest-frame emission from galaxies gets redshifted into the near-IR range not visible in i and z bands at higher redshifts.

By comparing the values of photometric and spectroscopic redshifts available from the photometric catalogues, we calculate the median accuracy of the photometric redshifts for both samples: the photometric redshift accuracy for COSMOS[6] is $(z_s - z_p)/(1 + z_s) = 0.007$, and for XMM-LSS $(z_s - z_p)/(1 + z_s) = 0.018$. The photometric precision of the COSMOS2020 catalogue is 1% at $i \approx 20\mathrm{AB}$ and 4% at $i \approx 26\mathrm{AB}$ (Weaver et al. 2022). For the XMM-LSS HSC-SSP photometric redshift catalogue the photometric accuracy is $\approx 3\%$ (Nishizawa et al. 2020).

2.5. Final sample used in the analysis

For the upcoming analysis of bent radio sources in Sect. 4, we reduced our samples to only include sources where it is possible to measure a BA, given the MIGHTEE-DR1 data at hand. We excluded sources without a host association, which we need for assigning the BA. The initial number of sources was reduced from 306 to 282 for XMM-LSS, and from 254 to 193 for COSMOS. We only include radio sources with two-sided jets or lobes where measuring the BA is possible. For the rest of the analysis, we only take into account these sub-samples of objects for which we can securely measure their BAs; that is, including only two-sided radio AGN for which the BA could be measured reliably. The final sample for XMM-LSS includes 217 sources, 189 (87%) of which have redshift available. The final sample for COSMOS includes 142 sources, 116 (82%) of which have redshift available (see Table 2).

We then cross-matched our radio samples with the X-ray galaxy groups in the XMM-LSS and COSMOS fields. As a proxy of the environment, we took the X-ray galaxy groups' mass and temperature (see Sect. 4.2).

For the COSMOS field, we used X-ray galaxy groups identified by *XMM-Newton* and Chandra in the 0.5–2 keV band (Gozaliasl et al. 2019, and in prep.), which provides coverage for the central $\sim 2.3\,\mathrm{deg}^2$ of the MIGHTEE-DR1 COSMOS mosaic with robust group identification up to a redshift of ~ 2. The X-ray galaxy group catalogue features 322 groups with group masses M_{200} ranging from $4 \times 10^{12}\,M_\odot$ to $3 \times 10^{14}\,M_\odot$, obtained with the X-ray luminosity L_X halo mass, $L_X - M_{200}$ scaling relation (Leauthaud et al. 2009). Similarly, the mean group temperature, T, was calculated with the $L_X - T$ scaling relation

(Finoguenov et al. 2007). The X-ray flux limit for the 0.5–2 keV band is $3 \times 10^{-16}\,\mathrm{erg\,s^{-1}\,cm^{-2}\,s^{-1}}$.

To determine which galaxies in the COSMOS sample are X-ray galaxy group members, we searched for all sources that are located within the virial radius r_{200} of the galaxy groups in COSMOS. This radius defines a sphere with an interior mean gas density 200 times the critical density of the Universe at the redshift of the group. We then checked if the redshift of the radio galaxy, z_galaxy, from our sample is at the same redshift range as the redshift of the galaxy group, z_group, given by the redshift accuracy of the COSMOS sample: $\Delta z = (z_\mathrm{galaxy} - z_\mathrm{group})/(1 + z_\mathrm{group}) \leq 0.007$. Finally, we cross-matched the right ascensions and declinations of all host galaxies that fulfil $r \leq r_{200}$ and $\Delta z \leq 0.007$ with the right ascensions and declinations of the known group members within $1''$. From this procedure, we find that, out of the 76 radio sources of the COSMOS sample that are inside the *XMM-Newton* and Chandra coverage, 19 are X-ray galaxy group members (25%).

For the XMM-LSS sample, we utilised *XMM-Newton* data from the 0.5–2 keV band that covers roughly the northern two thirds of the MIGHTEE-DR1 XMM-LSS mosaic. We analysed all *XMM-Newton* observations in overlap with the radio data that became public prior to 2023. We used XMMSAS[7] version 21.0.0 for the initial data reduction. For the XMM data screening, we followed the prescription outlined in Finoguenov et al. (2007) on data screening and background evaluation, with updates described in Bielby et al. (2010). To detect and study faint extended sources, we first removed the flux produced by the point sources, following Finoguenov et al. (2009). We detected the extended emission in the 0.5–2 keV mosaic image using the wavelet scales from 0.5 to 2 arcminutes. To identify X-ray galaxy groups, the redMaPPer pipeline (Rykoff et al. 2014) was employed (grey circles in Fig. 1) and was run in scanmode (e.g. as in Ider Chitham et al. 2020; Kluge et al. 2024). It utilised the photometric data from the 10th Data Release of the DECam Legacy Survey (DECaLS, Dey et al. 2019) and version 8 of the red-sequence Matched-filter Probabilistic Percolation cluster-finding algorithm code (redMaPPer, Rykoff et al. 2014). In contrast to the COSMOS field, which offers excellent spectrophotometric coverage, the quality of the photometric redshifts from DECaLS is insufficient to ensure robust group identification. We therefore visually confirmed which radio sources in the XMM-LSS field are located within the extended X-ray emission from the 0.5–2 keV *XMM-Newton* data (e.g. the right panel of Fig. 1) and calculated rough group properties using the redshifts of the host galaxies in our sample.

We performed a 2D spatial match between the locations of the radio sources in XMM-LSS and the X-ray extended data from *XMM-Newton* (green triangles in Fig. 1) and find that 79 out of the 183 (43%) radio sources of our BA sample lie within the X-ray coverage. By matching also in redshift space, using the extended X-ray sources from the redMaPPer pipeline, we find that 17 out of 183 radio sources (9%) lie inside X-ray galaxy groups (blue stars in Fig. 1). We note that, for a radio source to be considered an X-ray galaxy group member, the redshift of the host galaxy must lie within the redshift range of the extended X-ray source calculated from the redMaPPer pipeline, given by the redshift accuracy of the XMM-LSS sample: $\Delta z = (z_\mathrm{galaxy} - z_\mathrm{redMaPPer})/(1 + z_\mathrm{redMaPPer}) \leq 0.018$. Additionally, we excluded all group members associated with a group with richness $\lambda < 10$.

---

[6] This value agrees with the photometric redshift accuracy reported in Laigle et al. (2016).

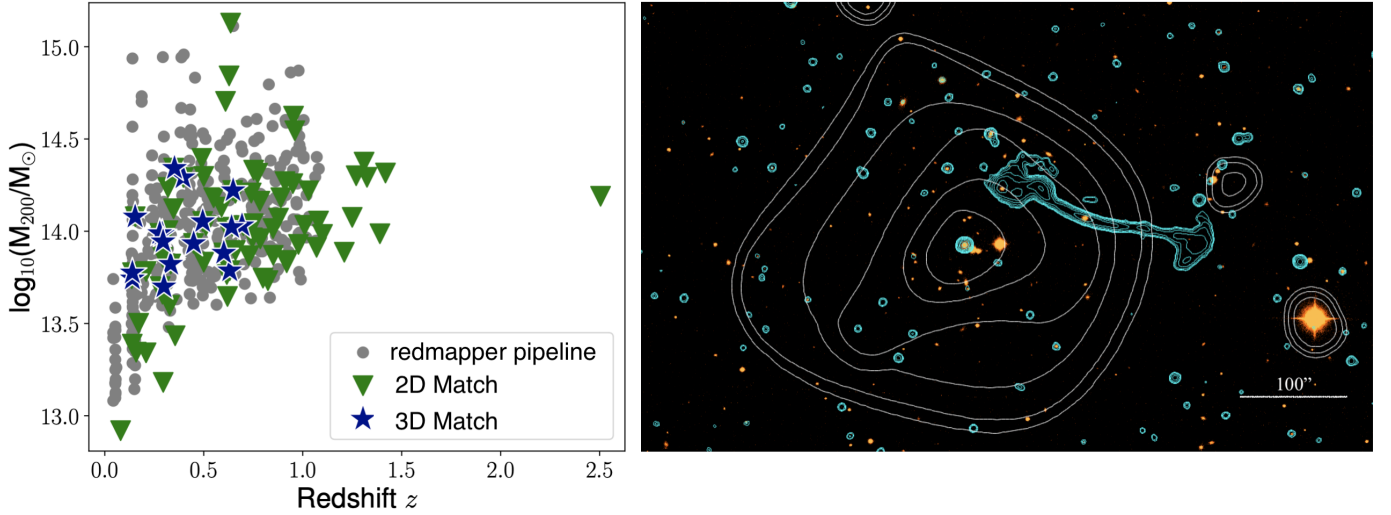[7] https://www.cosmos.esa.int/web/xmm-newton/sas

Fig. 1. Left: X-ray galaxy group masses, M_{200}, as a function of redshift in XMM-LSS, calculated with redMaPPer (grey circles), calculated with the redshift of sources in the XMM-LSS sample that visually coincide with the 0.5–2 keV extended X-ray emission (green triangles, 2D Match) and from cross-matching the X-ray galaxy groups from the '2D Match' to the ones from redMaPPer, given $\Delta z \leq 0.018$ (blue stars, 3D Match). Right: Example of a radio galaxy spatially coinciding with extended X-ray emission. The background is the SDSS i-band data, overlaid with MIGHTEE 8.9″ radio data at 3σ (cyan contours) and 0.5–2 keV extended X-ray emission (white contours). A scale of 100 arcsec in length is shown on the bottom right. This corresponds to 267 kpc at the redshift of the source 178, $z = 1.54$.

The halo masses, M_{200c}, for the 17 members in the XMM-LSS sample range from $5 \times 10^{13}\,M_\odot$ to $2 \times 10^{14}\,M_\odot$. The group with the lowest flux is found at $4 \times 10^{-15}\,\mathrm{erg\,s^{-1}\,cm^{-2}\,s^{-1}}$. Redshifts range from 0.34 to 0.7. The properties of the X-ray galaxy group of XMM-LSS and COSMOS are shown in Fig. 2 and discussed further in Sect. 5. We note that objects inside the X-ray coverage that are not members of galaxy groups might lie in mass halos below $<1.5(1 + z) \times 10^{13}\,M_\odot$ (for $z > 1$), not probed by our current X-ray data (see Gozaliasl et al. 2019).

3. Methods

3.1. Largest angular size

To obtain the values for the largest angular size for each source in our samples, we added the angular distances between the edges of the 3σ contours of the 5″ MIGHTEE data and the host position. For sources that have no clear lobe structure or no host information, we used the distance from edge to edge of the 3σ contours. We chose the 5″ MeerKAT map over the 8.9″ one, for more accurate measurements and to reduce blending effects.

Using the 5″ MIGHTEE data for angular size determination comes at the cost of potentially missing diffuse emission picked up by the more sensitive 8.9″ data. We find that on average the difference in angular size between the same objects of the two radio maps is $\approx$8″, close to the 8.9″ MIGHTEE beam size, suggesting that the difference is related to the beam. Thus, we are confident in using the angular size measurements from the 5″ map for our analysis.

3.2. The bending angle

Building on previous studies (e.g. Silverstein et al. 2017; Vardoulaki et al. 2021a,b; Garon et al. 2019; Golden-Marx et al. 2021), we used the BA, defined as the angle between the jets or lobes of two-sided radio sources, to study the distortion of the jet structure in relation to their large-scale environment. The BA

thus provides a quantitative way to measure the deviation from a straight line.

A completely straight source corresponds to a BA of 180°, while bent sources have an angle $< 180°$. We do not distinguish between upward and downward bending in the projected plane to the observer. Thus, the BA is a positive definite quantity between 0° and 180°, where radio sources are more bent the closer the BA is to 0°.

We measure the BA of each source in two ways: the first method, which we call the peak flux method, measures the angle between the vectors that originate in the host position and go to the peak flux in each jet, choosing the brightest pixel as the endpoint. We defined the peak flux as the hotspot in lobe structures, which is typically seen in FRII-type sources, or as the peak surface brightnesses, which are typically close to the centre in FRI-type jets. The second method, called the edge method, measures the angle between the two vectors going from the host position to the end of each 3σ contour, where the pixel that maximises the length of each vector is chosen at the 3σ contour. The quantitative differences between the two methods are presented in Sect. 4. In the following section, we discuss the usefulness and limitations of the BA methods as well as qualitative differences between the two methods of obtaining the BA.

3.3. The efficacy of the bending angle

We first want to address the limitations of using the BA, described in Sect. 3.2, as a method of investigating the distortion of jetted radio AGN. Similarly to the angular size, the measurement of the BA is affected by projection effects. Because we can only see radio sources as 2D projections on the sky, we cannot accurately account for the true shape the radio source has in 3D space. For example, a galaxy with a large BA seen from earth could be seen as having a small BA for an observer from another direction as the projected distance and angle between the jets change. This has nothing to do with the intrinsic or extrinsic properties of the radio source, but is purely geometrical, limited by the line of sight of the observer. An argument can be
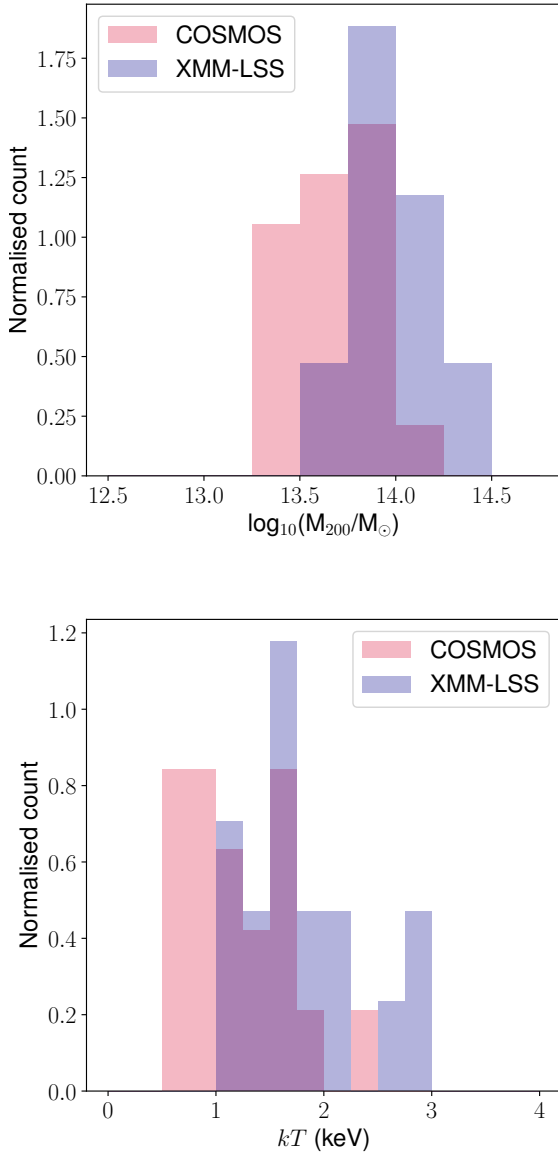
Fig. 2. Normalised count of the 19 extended radio AGN inside X-ray galaxy groups found in COSMOS (Gozaliasl et al. 2019, and in prep.) and the 17 galaxy groups in XMM-LSS associated with extended radio AGN and presented in Sect. 4.2. Top: Group masses M_{200} in $M_\odot$. The bin size is $0.25 \times \log_{10}(M_{200}/M_\odot)$. Bottom: Group temperatures, kT, in kilo-electronvolts. The bin size is 0.25 keV.

made that in an isotropic Universe, the error of the BA due to projection effects will average out over a large enough sample. An important consequence of this is that the BA is better suited for statistical analysis over large samples rather than a source-by-source approach. For this reason, we refrain from making strong statements about the most bent sources of our samples in our analysis and mostly distinguish between straight or slightly bent sources (BA > 160°) and moderately or very bent sources (BA ≤ 160°) in our statistics. The very bent sources (BA ≤ 100°) are discussed in more detail in the appendix. The value of 160° was chosen to allow for comparisons with the literature (see Sect. 5).

Another source of uncertainty from geometrical arguments is that positional errors of the peak surface brightness (or edge position) that is used to determine the BA will result in bigger errors for the BA the closer the peak surface brightness (or edge

position) is to the core. This is a concern for radio galaxies with small angular sizes, where small positional changes will result in larger changes in the BA. We therefore investigate the relation of size and BA. While the sources larger than 1 Mpc in our samples are typically not bent below 130°, we find no correlations between BA and angular or linear size. We should note that large sources (>1 Mpc) are rare, and consequently there are very few in our samples that cover small sky areas. Nevertheless, we do not observe a correlation between linear projected size and BA.

As we showed in Sect. 2, the characterisation of extended radio sources can be highly dependent on the radio survey's resolution, sensitivity, and frequency. For this reason, we measured the BA both from edges to radio core (edge method) and peak fluxes to radio core (peak flux method) for each source where possible. Using the edge method allows for the inclusion of more diffuse emission from FRI-type sources, which are subject to interaction with the environment. While sources with a typical FRII morphology will not show much difference between the two methods of obtaining the BA, FRI sources can show a stark difference between the two methods. This is because FRI sources have their peak surface brightness closer to the radio core, while their extended, diffuse emission can be subjected to deformation due to environmental effects. An advantage of measuring the BA with the peak flux method is that we expect it to be less affected by the selection effects related to observed frequency, sensitivity, and angular resolution of the survey, since the positions of the peak surface brightness should not change greatly over different radio datasets, in the case of well-defined radio jets. Nevertheless, for surveys with sub-arcsecond resolution, like the 3 GHz-COSMOS (Smolčić et al. 2017b) or LOFAR-VLBI observations (Sweijen et al. 2022), changes in the peak surface brightness are observed between ~6″ and sub-arcsecond resolutions. We note that with the edge method we should expect differences between low frequency and high frequency observations, with the former probing more extended and diffuse emission. Different telescope baselines will also have an effect on this. The BAs measured from the two methods follow the same distribution for both fields, suggesting that the BA is statistically consistent between the two methods. The medians of the absolute deviations between the angles of the peak flux method and the edge method are 5° and 6° for XMM-LSS and COSMOS, respectively.

4. Analysis and results of observational XMM-LSS and COSMOS MIGHTEE data

4.1. Bending angles

For sources where we can measure the BA with both methods, we calculated $\Delta BA = (BA_{PeakFlux} - BA_{Edge})/(1 + BA_{Edge})$ and found $\Delta BA < 0.01$ for 20% for all sources, $\Delta BA < 0.1$ for ~84% of sources in XMM-LSS, as well as $\Delta BA < 0.1$ for ~78% of sources in COSMOS. The median values for the objects with BAs from the two methods are listed in Tables 3 and 4. The scatter of the median is given by the 16th and 84th percentile. We note that the number of objects in Tables 3 and 4 differ because it was not possible to use both methods of BA measurement on all objects (e.g. lack of prominent peak flux for the peak flux method measurement).

The median values from Tables 3 and 4 show that the BAs from the two methods yield similar median and scatter values. A Kolmogorov-Smirnov test (K-S test) with a significance level of 0.05 confirms that the BAs from the two methods come

Table 3. Median BAs from the peak flux method.

Sample	N	Bending angle (deg)		
		Median$_{16\%}^{84\%}$	Min	Max
XMM-LSS	214	$168.0_{146.1}^{175.0}$	55	180
COSMOS	112	$168.0_{141.3}^{175.2}$	46	180
Combined	326	$168.0_{145.0}^{175.0}$	46	180

Notes. Here, we present all sources that we could measure a BA, including those outside X-ray galaxy groups.

Table 4. Median BAs from the edge method.

Sample	N	Bending angle (deg)		
		Median$_{16\%}^{84\%}$	Min	Max
XMM-LSS	217	$168.0_{138.6}^{176.0}$	16	180
COSMOS	142	$166.0_{135.9}^{177.0}$	45	180
Combined	359	$167.5_{137.0}^{176.0}$	16	180

Notes. Here, we present all sources that we could measure a BA, including those outside X-ray galaxy groups.

Table 5. Degree of bending for sources in the XMM-LSS and COSMOS samples.

	XMM-LSS		COSMOS	
	N	Median$_{16\%}^{84\%}$	N	Median$_{16\%}^{84\%}$
Straight/slightly bent	139	$174.0_{167.0}^{177.0}$	88	$174.0_{167.0}^{178.0}$
(BA > 160°)	(~64%)		(~57%)	
Moderately bent	71	$144.0_{120.4}^{155.0}$	54	$147.0_{120.5}^{158.0}$
(100° < BA ≤ 160°)	(~33%)		(~38%)	
Very bent	7	$83.0_{22.7}^{97.0}$	6	$63.0_{50.6}^{73.4}$
(BA ≤ 100°)	(~3%)		(~4%)	

Notes. Here, we present all sources that we could measure a BA, including those outside X-ray galaxy groups.

from the same distribution for both samples (XMM-LSS: K-S statistic = 0.1, p-value = 0.25; COSMOS: K-S statistic = 0.09, p-value = 0.77). In Table 5, we show the number of sources in each sample that are straight or slightly bent (BA > 160°), moderately bent (100° < BA ≤ 160°), and very bent (BA ≤ 100°), as well as their median BA values. We find that for both samples well over 50% of sources are straight or slightly bent, with only a few very bent sources in each sample. For the rest of this work, we use the BAs obtained from the edge method unless stated otherwise.

4.2. Bending angle versus large-scale environment

To investigate the relation between the BA and the large-scale environment, we cross-correlated the sources in our sample to the X-ray galaxy groups (see Sect. 2.5) to find relations between the BA and group properties, such as group mass and temperature, and to understand the role the large-scale environment probed by galaxy groups plays in shaping the radio structure of extended radio AGN. We constrained the radio-source sample to

the same area coverage as the X-ray observations, which cover ~2.3 deg^2 in COSMOS and ~7 deg^2 in XMM-LSS.

We find a trend with redshift for objects that are members of X-ray galaxy groups; that is, a larger number of bent sources (BA ≤ 160°) at lower redshifts. We applied a halo mass cut of $\log_{10}(M_{200}/M_{\odot}) > 13.5$, to probe the same group population at all redshifts (see Vardoulaki et al. 2023), and found that in the COSMOS sample at $z \leq 0.5$ we have $\langle BA \rangle = 141° \pm 39°$ (five objects), while at $z > 0.5$ the $\langle BA \rangle = 154° \pm 16°$ (two sources). For XMM-LSS, at $z \leq 0.5$, we have $\langle BA \rangle = 95° \pm 49°$ (7 objects), while at $z > 0.5$ the $\langle BA \rangle = 130° \pm 8°$ (two sources). In the following, we discuss separately the bent sources in COSMOS and XMM-LSS. Accounting for very bent sources (<100°), these are located at $z \leq 0.5$ in both samples. Only source 252 in COSMOS is below the halo mass cut, while the other very bent source in COSMOS (source 247) and the two in XMM-LSS (sources 1 and 200) are above the cut.

4.2.1. Group members in COSMOS

We find 19 (25%) bent sources inside X-ray galaxy groups and 57 outside (see Table 2). For the 19 sources in the COSMOS sample that are inside X-ray groups, we find that the median BA (with the 16th and 84th percentile) is $156.0_{117.7}^{171.1}$ degrees, while the median BA for the 57 sources that are not considered group members and are in the same area coverage as *XMM-Newton* and Chandra is $168.0_{140.0}^{177.0}$ degrees.

In the top panel of Fig. 3, we plot the BA for radio sources in the COSMOS X-ray galaxy groups in relation to host stellar mass as red pentagons. The stellar mass was obtained from Gozaliasl et al. (2019). We do not see a correlation between BA and stellar mass for the COSMOS X-ray galaxy group members, although bent and very bent sources have $M_{\star} > 10^{11} M_{\odot}$. Brightest group galaxies (BGGs) are highlighted by filled-out symbols. The 17 out of the 19 members from our sample tend to occupy the high stellar mass end at their respective redshift. This is expected since radio AGN are more likely to be hosted by more massive galaxies (e.g. Magliocchetti 2022). We note that objects 221 and 225 in COSMOS do not have a stellar mass measurement based on the currently available data.

In the middle panel of Fig. 3, we plot the BAs of the members of the X-ray groups in COSMOS against the corresponding halo mass, expressed in terms of M_{200}, which is the mass of the group inside the virial radius r_{200}. We see no clear trend between group mass and the BA, possibly due to the low sample size of 19 objects. Also, we do not observe a significant difference between the BAs of BGGs and non-BGGs.

The bottom panel in Fig. 3 shows the BA as a function of the mean group temperature, kT, in kilo-electronvolts. We find no strong correlation between the BA and kT. Very bent sources show low temperatures, while there is a lack of very bent sources at higher temperatures. The Spearman test between BA and temperature gives only a correlation coefficient of $r_s = 0.19$ with a p-value of 0.44. This corresponds to a weak to no correlation with no evidence to reject the null hypothesis, suggesting that the correlation is not physical.

We also see that there is no source in COSMOS, for which we could robustly measure a BA, located in a galaxy group beyond a redshift of 1.2. This is likely because of the low numbers of high redshift sources in our sample and the low number of high redshift X-ray galaxy groups. We acknowledge the small sample sizes for some subsets (e.g. high-redshift or very bent sources in galaxy groups). Expanding the dataset to additional fields (e.g. ELAIS-S1) or wider sky areas (assuming a wealth
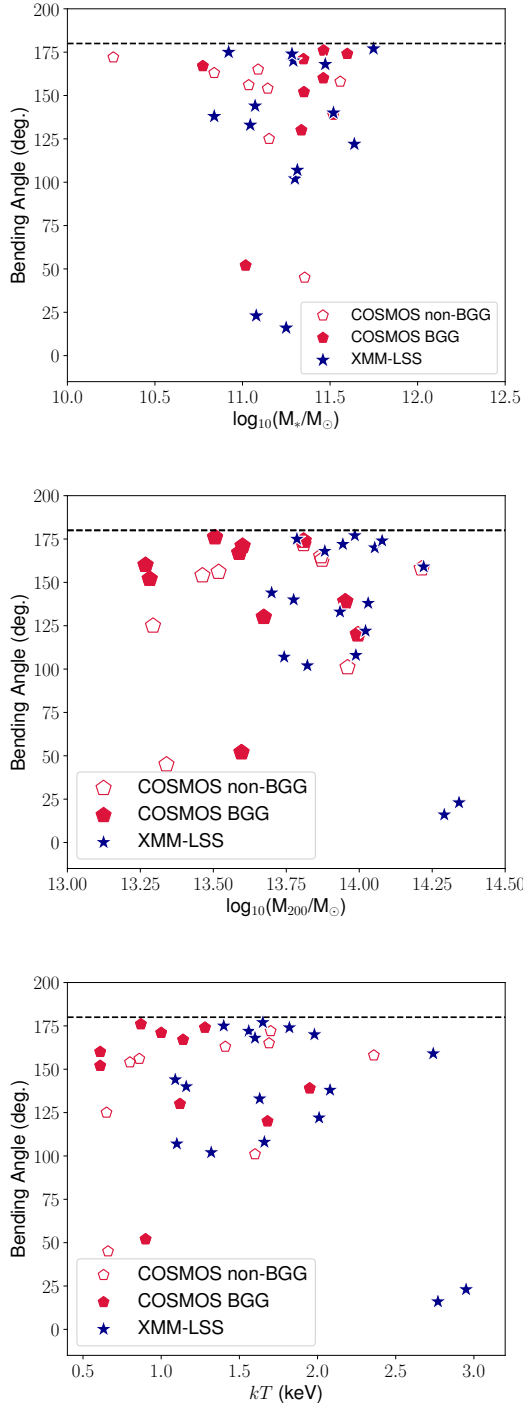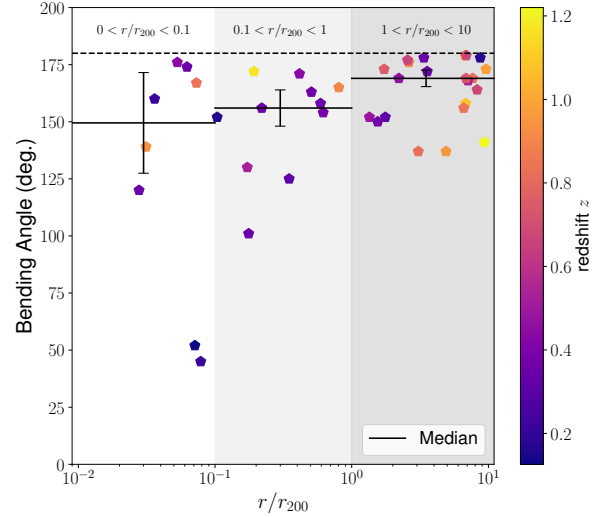
Fig. 4. Bending angle in degrees of radio sources in X-ray galaxy groups as a function of distance to the group centre in units of r_{200} for the COSMOS field. We distinguish between the core region ($0 < r/r_{200} < 0.1$), the inner region ($0.1 < r/r_{200} < 1$) and the outer region ($1 < r/r_{200} < 10$) of the groups. The black lines and error bars show the median and standard median error of the BAs in the regions. The redshift of the radio sources is shown with a colour bar. The dashed line at 180° indicates a straight source.

Fig. 3. Bending angle in degrees as a function of the stellar mass, $M_\star$ (top), of the X-ray galaxy group mass, M_{200} (middle), and of the X-ray galaxy group temperature, kT, in kilo-electronvolts (bottom). In all panels, red pentagons denote COSMOS objects and filled blue stars denote XMM-LSS objects. In the COSMOS sample, BGGs are shown as filled symbols. For the XMM-LSS sample, the BGG information is not available at the time of writing due to the different methods the X-ray groups were defined (see Sect. 2.5). The dashed line at 180° indicates a straight source.

of multi-wavelength observations) could address this limitation, but this is out of the scope of the current work. Nevertheless, literature studies, show that bent sources in clusters exist at high redshifts. For example, the study of Golden-Marx et al. (2021) in an area of 300 deg², finds 36 bent radio sources in clusters

up to $z \sim 2.2$. Furthermore, Hale et al. (2018) suggest that AGN could occupy less massive groups at $z > 1$, which require high sensitivity X-ray observations (also see Vardoulaki et al. 2023, for further discussion).

To investigate the relation between BA and distance from the X-ray group centre in the COSMOS field, we plot in Fig. 4 the BAs against the projected distance r of the radio sources to the group centre, normalised by the virial radius r_{200}. The core region typically covers the range of $0 < r/r_{200} < 0.1$ (e.g. Navarro et al. 1995, 1997; Navarro 1996). The range $0.1 < r/r_{200} < 1$ is deemed the inner region of the X-ray galaxy group. We also include all sources out to $r/r_{200} < 10$ (and $\Delta z \pm 0.007$) from the centre, named the outer region. We do not consider these galaxies as group members, because they lie beyond the virial radius of r_{200} and were also not assigned a membership based on the studies of Gozaliasl et al. (2019). The reason we include them in this plot is to investigate trends in the periphery of the X-ray galaxy groups. We find that the two most bent sources in the COSMOS sample are located in the core region of their corresponding X-ray galaxy group. We also find that the BA moderately correlates with distance to the group centre, with strong evidence to reject the null hypothesis (Spearman test: $r_s = 0.4$, p-value = 0.01). Similarly, we find that the redshift for sources in galaxy groups both moderately correlate with the BA ($r_s = 0.55$, p-value = 0.02) and distance to the group centre ($r_s = 0.46$, p-value = 0.0003).

To look for emerging trends in the relatively low sample size of X-ray galaxy group members, we split the 19 sources into two sub-samples of sources that are straight or slightly bent (BA > 160°) and moderately or very bent sources (BA ≤ 160°). In Table 6, we compile the median values of the group properties for straight versus bent radio sources in groups.

We report that 12 out of 19 (63%) sources in groups in the COSMOS field have a BA ≤ 160°. For these sources, we observe lower median values for X-ray group redshift, halo mass and mean group temperature, as well as a smaller distance to the

Table 6. Median X-ray group properties and percentiles for straight (BA > 160 deg) and bent (BA ≤ 160 deg) group members in the COSMOS sample.

BA	N			Median$_{16\%}^{84\%}$			
(deg)		BA/deg	z	$\log_{10}(M_{200}/M_\odot)$	r/r_{200}	kT/keV	N_{gal}
>160	7	$171.0_{164.9}^{174.1}$	$0.44_{0.36}^{0.90}$	$13.81_{13.59}^{13.87}$	$0.19_{0.06}^{0.52}$	$1.28_{0.99}^{1.69}$	20.0_{11}^{83}
≤160	12	$134.5_{89.2}^{156.5}$	$0.34_{0.21}^{0.41}$	$13.56_{13.29}^{13.97}$	$0.14_{0.03}^{0.41}$	$0.88_{0.64}^{1.74}$	22.5_{7}^{117}

Notes. BA is the bending angle in degrees; z the redshift; M_{200} is the mass of the galaxy group in $M_\odot$; r is the distance from the X-ray galaxy group centre normalised to r_{200}; kT is the temperature of the group in kilo-electronvolts; and N_{gal} is the number of galaxies that are members of the X-ray galaxy group.

group centre, but only within the scatter values of the medians. There is no clear divide between the properties of bent and straight sources in groups; however, there is a large overlap in the distributions of the two samples. The median number of group members with $M_\star > 10^9 \, M_\odot$ for straight and bent sources are comparable, with the number of galaxies that are members of the groups being $N_{\mathrm{gal}} = 20.0_{11}^{83}$ for straight sources and $N_{\mathrm{gal}} = 22.5_7^{117}$ for bent sources.

4.2.2. Group members in XMM-LSS

For the XMM-LSS field, we obtain 17 (10%) sources inside X-ray galaxy groups and 149 outside X-ray galaxy groups. For the 17 sources in the XMM-LSS sample that are inside X-ray groups, we find that the median BA is $140.0_{104.8}^{172.9}$ degrees, while the median BA for sources that are not considered group members and that are also covered by *XMM-Newton* is $169.0_{146.0}^{176.0}$ degrees.

In Fig. 3, we show the BA as a function of stellar (top panel) and halo mass (middle panel), where XMM-LSS sources are plotted as filled blue stars. We note that sources 5, 60 and 84 do not have a stellar mass measurement based on the currently available data. We see that the two most bent sources in XMM-LSS are associated with more massive groups ($M_{200} > 10^{14} \, M_\odot$) and with massive hosts ($M_\star > 10^{11} \, M_\odot$) while the other sources do not show any trend between BA and group or stellar mass. We note that most sources, barring two (sources 49 and 57), are associated with massive hosts ($M_\star > 10^{11} \, M_\odot$), similar to COSMOS, which has three group members below $10^{11} \, M_\odot$. We note that the halo mass parameter space is different from that of the COSMOS field, with the latter probing halo masses below $10^{13.6} \, M_\odot$.

The bottom panel in Fig. 3 shows the BA in XMM-LSS as a function of the mean group temperature, kT, in kilo-electronvolts. We find no strong correlation between the BA and kT. Very bent sources show high temperatures, contrary to what is seen from the COSMOS sources. We discuss this further in Sect. 6 and in the appendix.

In Fig. 5, we show the BA as a function of distance to the group centre in units of r_{200}. Similarly to Fig. 4, we distinguish between the core and inner region of the X-ray group, but do not include sources beyond r_{200}, due to the poorer photometric data available for XMM-LSS, compared to COSMOS (see Sect. 2.5). This means we could not define in a similar manner, and robustly, the sources at the outer region of galaxy groups in XMM-LSS, as we did in COSMOS. We find that the median BA of group members of the core region is $\mathrm{BA}_{\mathrm{med}} = 124.0_{107.5}^{142.1}$ and $\mathrm{BA}_{\mathrm{med}} = 159.0_{95.7}^{174.1}$ for members of the inner region. In contrast to the COSMOS group members, the two most bent sources in XMM-LSS are located in the 'inner region' rather than the core
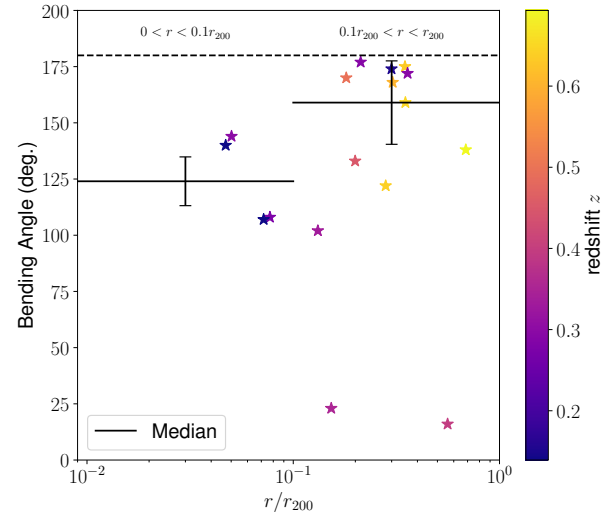

Fig. 5. Bending angle in degrees of radio sources in X-ray galaxy groups as a function of distance to the group centre in units of r_{200} for the XMM-LSS field. We distinguish between the core region ($0 < r/r_{200} < 0.1$) and the inner region ($0.1 < r/r_{200} < 1$) of the groups. The black lines and error bars show the median and standard median error of the BAs in the regions. The redshift of the radio sources is shown with a colour bar. The dashed line at 180° indicates a straight source.

region of groups. We note that the two very bent sources are narrow-angle tail (NAT) sources, and probably in-falling to the group centre. We discuss these further in the appendix.

In Table 7, we show the median group properties for sources in XMM-LSS that are straight or slightly bent (BA > 160°) and for bent sources (BA ≤ 160°). We see that 11 out of 17 group members have a BA ≤ 160°. We find only slight differences between the median redshift, halo mass and mean group temperature for straight and bent radio sources, with overlapping distributions. The median distance to the group centre for bent sources is $0.15 \, r/r_{200}$, which is smaller by a factor of two than the value for straight and slightly bent sources.

In Table 8, we compile the median BAs for the group members in the core and inner regions of X-ray galaxy groups and also compare the BAs of all group members to the radio sources that are not considered X-ray group members (field sources). For both fields, we find that sources located in the core region are more bent (22% more bent in XMM-LSS and 4% more bent in COSMOS) than the sources in the inner region of galaxy groups. Similarly, group members are more bent (17% more bent in XMM-LSS and 7% more bent in COSMOS) than the sources located in the field. The two most bent sources in each sample

Table 7. Median X-ray group properties and percentiles for straight (BA > 160 deg) and bent (BA ≤ 160 deg) group members in the XMM-LSS sample.

BA	N			Median$_{16\%}^{84\%}$		
(deg)		BA/deg	z	$\log_{10}(M_{200}/M_\odot)$	r/r_{200}	kT/keV
>160	6	$173.0_{169.6}^{175.4}$	$0.39_{0.26}^{0.61}$	$13.96_{13.86}^{14.06}$	$0.30_{0.21}^{0.35}$	$1.63_{1.53}^{1.85}$
≤160	11	$122.0_{70.4}^{141.6}$	$0.35_{0.22}^{0.65}$	$13.99_{13.76}^{14.25}$	$0.15_{0.06}^{0.43}$	$1.66_{1.14}^{2.75}$

Notes. BA is the bending angle in degrees; z the redshift; M_{200} is the mass of the galaxy group in $M_\odot$; r is the distance from the X-ray galaxy group centre normalised to r_{200}; kT is the temperature of the group in kilo-electronvolts; and N_{gal} is the number of radio sources.

Table 8. Bending angles for group and field sources in the same area coverage.

Field	N	Bending angle (deg)		
		Median$_{16\%}^{84\%}$	Min	Max
Core region ($0 < r/r_{200} < 0.1$)				
XMM-LSS	4	$124.0_{107.5}^{142.1}$	107	144
COSMOS	8	$149.5_{128.0}^{167.4}$	45	176
Inner region ($0.1 < r/r_{200} < 1$)				
XMM-LSS	13	$159.0_{95.7}^{174.1}$	16	177
COSMOS	11	$156.0_{128.0}^{167.4}$	101	172
Group Members				
XMM-LSS	17	$140.0_{104.8}^{172.9}$	16	177
COSMOS	19	$156.0_{117.7}^{171.1}$	45	176
Field Sources				
XMM-LSS	149	$169.0_{146.0}^{176.0}$	83	180
COSMOS	57	$168.0_{140.8}^{177.0}$	102	180

are located in galaxy groups. These four sources in particular will be further discussed in the appendix.

5. Discussion

5.1. Radio size and luminosity of X-ray galaxy group members

We investigated relations between the physical properties of X-ray galaxy group members in XMM-LSS and COSMOS. The sky coverage of MIGHTEE-DR1 observations is 14.4 deg^2 for XMM-LSS and 4.2 deg^2 for COSMOS. From our total samples – that is, all sources within the DR1 mosaics for which we measured the BA – we obtain 15.07 sources/deg^2 for XMM-LSS and 33.81 sources/deg^2 in COSMOS. Our results suggest that COSMOS is a more densely populated field than XMM-LSS. Literature studies of bent radio AGN, and in particular the study of Golden-Marx et al. (2019), who targeted clusters of galaxies selected from the VLA FIRST radio survey (Helfand et al. 2015; Becker et al. 1995, beam size: 5″, rms: ∼150 μJy/beam) and the study of Wing & Blanton (2011), indicates an expected number of bent double sources (BA ≤ 160°) of the order of 646 in 300 deg^2, or 2.12 sources/deg^2. The increased

source count per square degree in our samples is attributed to the high sensitivity of the MIGHTEE survey, the inclusion of sources with BA > 160° and the larger redshift range (0.01 < z < 3.2). If we constrain our samples to bent group members (BA ≤ 160°) in the redshift range of Golden-Marx et al. (2021) of 0.35 < z < 2.2, we get 0.71 sources/deg^2 in XMM-LSS and 1.74 sources/deg^2 in COSMOS, compared to the 0.12 sources/deg^2 Golden-Marx et al. (2021) find from the sample of 36 high-z bent sources in clusters.

Golden-Marx et al. (2021) investigate the parameter space 36 < BA (deg) ≤ 160, linear size of ∼120–600 arcsec, $10^{24.7}$ < $L_{1.4\,GHz}/[W\,Hz^{-1}]$ < $10^{27.7}$. Other studies, such as that of Garon et al. (2019), find 988 bent radio sources (BA ≤ 160°) in 10 575 deg^2 below redshift z < 0.8, which gives ∼0.1 sources/deg^2. Garon et al. (2019) investigate the parameter space 0.02 < z < 0.8, 0.2 < BA (deg) < 180 (values changed to match our conversion), angular size 0.2–1.3 arcmin, and L_{min} = 2×10^{23} W Hz^{-1}, while they probe clusters with masses M_{500} > $5 \times 10^{14}\,M_\odot$. We attribute the discrepancy in the findings to the different parameter space probed. Restricting our sample to z ≤ 0.8 yields ∼1 sources/deg^2 for XMM-LSS, and ∼4 sources/deg^2 for COSMOS. Finally, Mingo et al. (2019) identify 459 bent-tailed in LoTSS below redshift z < 0.4, covering 424 deg^2, which gives ∼1 source/deg^2. Considering only sources within clusters and their match fraction of ∼50%, Mingo et al. (2019) find 0.54 bent-tailed sources/deg^2, reportedly WATs and NATs, including core-jet sources. A direct comparison to our sample is not possible. The interesting result is that in COSMOS we find a larger number of bent sources per square degree than in other fields and studies. COSMOS is known to have several overdensities in the redshift range covered by our study (see Scoville et al. 2013). We discuss this point further down.

We further investigate the reason we do not find bent radio AGN above z = 1.2 in our samples of group members. Golden-Marx et al. (2021) find a total of nine bent, double-lobed radio galaxies above z = 1.2 in clusters in 300 deg^2, which corresponds to 0.03 bent double sources/deg^2 for z ≥ 1.2. From this, we should expect to find 0.43 bent double sources/deg^2 in XMM-LSS and 0.13 bent double sources/deg^2 in COSMOS for z ≥ 1.2. From this comparison, we conclude that bent radio AGN at z ≥ 1.2 are rare and that large sky coverage is required to find them.

By comparing the linear projected size and radio luminosity of the COSMOS and XMM-LSS X-ray galaxy group members, we find a moderate correlation between those quantities, where r_s = 0.46, p-value = 0.05 for COSMOS and r_s = 0.44, p-value = 0.08 for XMM-LSS. This also corresponds to a moderate correlation between radio luminosity and linear size, but with weaker evidence to reject the null hypothesis, likely owing

to the smaller sample size. If we compare the whole COSMOS and XMM-LSS samples, the correlation between linear size and luminosity is stronger for galaxy group members than for the whole sample. Our results agree with the literature and the moderate correlation found by Golden-Marx et al. (2021).

We note that except for a giant radio galaxy (GRG) that we find in COSMOS (Source 178; see also Delhaize et al. 2021), the bent sources in groups and clusters have radio sizes between 100–800 kpc[8]. The GRG in COSMOS recently reported in Charlton et al. (2025) is located at the north edge of the coverage of the DR1 mosaic and missing half the jet structure towards the north, and thus does not fulfil our criteria for the measurement of the BA; that is, two-sided radio structures. Malarecki et al. (2015) report that hosts of GRGs are usually found in environments of higher galaxy density, similar to group environments. However, we note that out of the 11 GRGs (2 sources in COSMOS and 9 sources in XMM-LSS), we find in our samples inside the X-ray coverage, only Source 178 in COSMOS is inside a group environment ($M_{200} \sim 2 \times 10^{13}\,M_\odot$). Recently, Neronov et al. (2024) explored the reason why GRGs such as Porphyrion with a size of 7 Mpc, grow so large. They argue that such systems can expand inside filaments and their jets trace a very high-energy gamma-ray beam emitted by AGN.

Interestingly, sources larger than 500 kpc, which are members of X-ray galaxy groups, are less bent by ∼25% on average compared to sources smaller than that. While there is no statistically significant correlation between BA and size, we note that we find a moderate correlation with strong evidence to reject the null hypothesis between the distance from the group centre and linear size for the XMM-LSS group members ($r_s = 0.60$, p-value = 0.01; see the bottom panel of Fig. 6). This could indicate that, as the ICM density increases towards the centre of the group, the expansion of radio jets is hindered. Moravec et al. (2019, 2020) find such a relationship between radio size and distance from cluster centres from observations and the self-similar jet model from Falle (1991), arguing that the radio size depends on jet power, the lifetime of the source, and the density of the surrounding medium:

$$D = c \left(\frac{t^3 Q_{\mathrm{jet}}}{\rho} \right)^{1/(5-\alpha)}, \tag{1}$$

with D the size of the radio source, c a dimensionless constant encompassing the adiabatic index of the surrounding gas and the opening angle of the jets, Q_{jet} the jet power, ρ the density of the environment, and t the lifetime of the source. ρ is typically modelled by a radial profile of the form $\rho = \rho_0 r^{-\alpha}$, where r is the distance from the source.

Under the assumption of no strong radial density gradients on jet scales, α becomes 0 and ρ only depends on the distance to the cluster centre. However, as is seen in the top panel of Fig. 6, no correlation between distance from the group centre and radio size is found for our COSMOS group members. Golden-Marx et al. (2021) also find no agreement with the relationship of Moravec et al. (2019), suggesting that the relationship between size and distance from group/cluster centre is not straightforward. We further discuss Eq. (1) by estimating Q_{jet} and ρ_{ICM} in Sect. 5.4.

5.2. X-ray galaxy group properties

While we can compare the intrinsic host properties of the members of X-ray galaxy groups, it is not trivial to compare the group
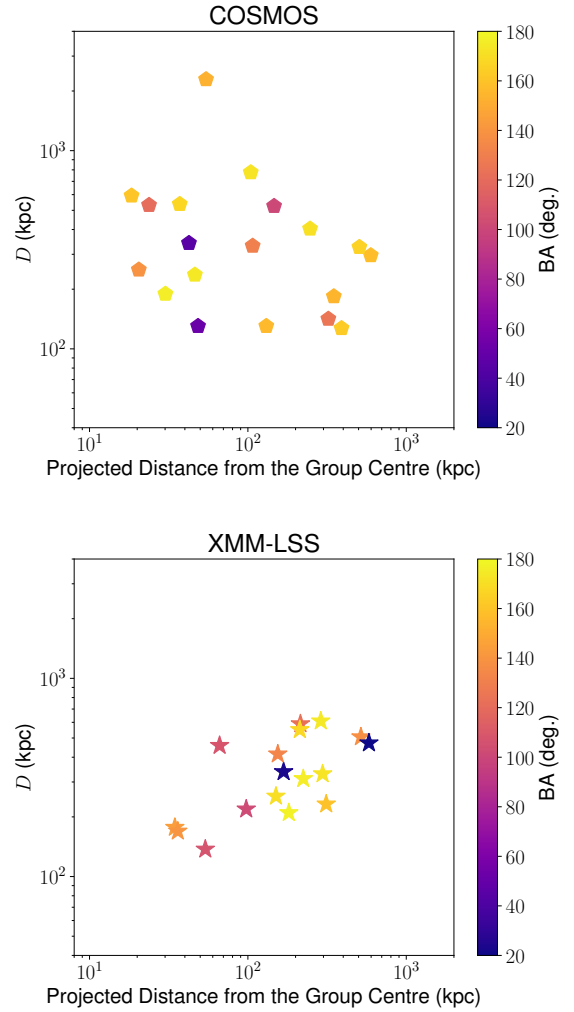
---

[8] We define GRGs as sources with a linear projected size ≥ 1 Mpc.

Fig. 6. Projected linear size, D, of group members in kiloparsecs as a function of projected distance from the group centre in kiloparsecs. The BA of the radio sources are shown by a colour scale. Top: COSMOS group members. Bottom: XMM-LSS group members.

properties from X-ray galaxy groups found for COSMOS and XMM-LSS. In addition to the differences in spectrophotometric data quality available for the fields (see Sect. 2.5), the surveys we utilise for the COSMOS groups (see Gozaliasl et al. 2019, and in prep.) have a lower flux limit than the survey conducted for XMM-LSS (see Gozaliasl et al. 2014), resulting in lower halo mass and temperature ranges in COSMOS.

Since we have a robust catalogue of 322 X-ray galaxy groups available for COSMOS (Gozaliasl et al. 2019, and in prep.), we can compare the ranges of all galaxy groups in COSMOS to the 17 groups in XMM-LSS that host bent radio sources of our samples, which we show in Fig. 2. While this comparison cannot show the differences in distribution for all galaxy groups of the two fields, we can confirm that the COSMOS groups are distributed at lower halo masses and temperatures compared to those in XMM-LSS which host bent radio sources, owing to the difference in flux limit.

In a relaxed group, the gas density will increase as the distance to the group centre decreases (e.g. Ascasibar et al. 2003). Thus, jet bending due to the movement of a radio galaxy through the group medium will be more pronounced for galaxies that are in closer proximity to the group centre. This is shown in the study of Garon et al. (2019), who investigated 4304 radio

galaxies in optically selected galaxy clusters, and find that the jet bending becomes less severe the further the galaxy is from the cluster core. In our study, we see, on average, a similar behaviour (except for the two NATs in XMM-LSS). As we summarise in Table 8, we find that the median BA for sources located in X-ray galaxy groups is lower than for the sources we do not consider group members, with the lowest median BAs found in the core region ($r/r_{200} < 0.1$) of the groups. The scatter of these values is large, ranging from 30° to 80° between the 16th and 84th percentiles, and straight or slightly bent objects (BA > 160°) are also found in X-ray galaxy groups. A K-S test between the BAs for group members and field sources shows that the BA distribution is different between members of the field and of groups, (K-S statistic = 0.53, p-value = 0.02 in XMM-LSS and K-S statistic =0.42, p-value = 0.07 in COSMOS), though this is limited by the small number of group members. Even so, for both the XMM-LSS and COSMOS sample we find that ~64% of all group members have a BA ≤ 160°, while only ~34% of all field sources have a BA ≤ 160°.

As Table 8 shows, we still find sources with BAs down to 83° in the field. A reasonable question would be why we find bent sources at all if they are not located in a dense group or cluster environment. The reason can be attributed to the sensitivity of the current X-ray observations. In particular, for COSMOS, we can only detect X-ray galaxy groups with halo masses ≈1.5(1 + z) × 10^13 M_⊙ (Vardoulaki et al. 2019). Additionally, a good photometric catalogue plays an important role in the robust membership assignment of the galaxies in groups. As we have discussed in Sect. 2.5, the method of identifying galaxies as members of a group in XMM-LSS only allows us to assign a secure membership to 17 bent radio AGN. Thus, bent sources that are not members of groups can be used as tracers for groups and clusters (e.g. Hintzen 1984; Blanton et al. 2000; Smolčić et al. 2007; Mingo et al. 2019; Vardoulaki et al. 2019). Another reason could be that a radio galaxy interacted with a group in the past and now is located outside the virial radius of the group (e.g. Wetzel et al. 2014). Bent sources like WATs can also be located in filaments of the cosmic web (e.g. Edwards et al. 2010; Garon et al. 2019; Vardoulaki et al. 2021b; Morris et al. 2022) instead.

Ignoring the very bent sources located in the X-ray galaxy groups (BA ≤ 100°), which are discussed in more detail in the appendix, we find no trend between BA and group halo mass or temperature for either the COSMOS or the XMM-LSS samples (see Figs. 3, 4 and 5). We again compare this to the large sample of 4304 bent radio galaxies located in optically selected galaxy clusters (Garon et al. 2019), who find that more bent sources are located in more massive clusters with higher ICM pressures. One of the reasons we might not obtain this trend is because our sample size of group members is too small to find any significant correlations. Another explanation is the different parameter space of Garon et al. (2019), who examine sources in galaxy clusters ranging from $M_{500} = 5 \times 10^{14} M_⊙$ to $30 \times 10^{14} M_⊙$, while the galaxy groups that host the bent sources of our samples have halo masses $M_{500} = 2 \times 10^{13} M_⊙$ to $1 \times 10^{14} M_⊙$ in COSMOS and $M_{500} = 4 \times 10^{13} M_⊙$ to $2 \times 10^{14} M_⊙$ in XMM-LSS. The galaxy group masses M_{200} from the X-ray galaxy groups are converted to M_{500} using the COLOSSUS code (Diemer 2018, COsmology, haLO and large-Scale StrUcture toolS). The halo mass of groups and clusters is related to the dispersion velocities of their members (e.g. Saro et al. 2013), so we expect galaxies to move faster through the ICM in more massive groups or clusters. Similarly, scaling relations between dispersion velocities of galaxies and group temperature show that statistically, hotter group environ-

ments are indicative of members that move through the ICM with high velocities (e.g. Lubin & Bahcall 1993).

As we discuss in the upcoming section, the halo mass is correlated to the ICM pressure of the group or cluster. Both higher galaxy velocities through the ICM and higher ICM pressures should promote jet bending through ram pressure that is exerted on the jets (Begelman et al. 1979). At first glance, it is therefore unexpected to find no correlation between BA and halo mass or temperature. This begs the question if the halo masses and temperatures we observe in XMM-LSS and COSMOS are too small to cause ram pressure-induced jet bending. Mguda et al. (2015) find from simulations that radio sources bent due to ram pressure are equally found in halo masses above and below $10^{14.5} M_⊙$, but that this comes from the fact that the lower mass clusters far outnumber higher mass clusters. In other words, more massive clusters are more likely to host bent sources due to ram pressure, but are rare, while less massive clusters are less likely to host bent sources due to ram pressure, but are not rare. Since all of the X-ray galaxy groups in our study have masses below $10^{14.5} M_⊙$, we are disproportionately affected by the small sample size of groups. However, studies have shown that the difference in properties of clusters and groups is not a simple matter of up- or downscaling (e.g. Sanderson et al. 2003; Borgani et al. 2004; Gaspari et al. 2011). The heating due to feedback from AGN (see Fabian 2012, for a review) has a bigger impact on the smaller halos of groups, resulting in a steeper $L_X - T$ scaling relation than for clusters (e.g. Helsdon & Ponman 2000; Magliocchetti 2022). This is connected to a flattening in the gas density profile in groups with temperatures below 3–4 keV (Ponman et al. 1999), which applies to the groups that host the bent sources of our samples. This can be related to the results of Smolčić et al. (2011) and Vardoulaki et al. (2023), which show that sources remain active inside galaxy groups compared to the field. In more massive clusters, the effects of heating from feedback will be less severe than for groups. This makes a direct comparison to massive cluster environments difficult. We therefore investigated the relation of jet bending and ram pressure more directly.

5.3. Ram pressure as a reason for jet bending in galaxy groups

As was discussed above, we expect jets to bend in group environments because of the ram pressure the ICM exerts on the jets as they move through the dense group medium (Begelman et al. 1979; Jones & Owen 1979). This pressure is expressed as $P_{ram} = \rho_{ICM} v_{gal}^2$, where ρ_{ICM} is the density of the ICM and v_{gal} is the relative velocity between the galaxy and the ICM gas particles (Jones & Owen 1979). The curvature of the jets in relation to the ram pressure can be expressed by:

$$\frac{\rho_{ICM} v_{gal}^2}{h} = \frac{\rho_j v_j^2}{R}, \tag{2}$$

where ρ_j and v_j are the gas density and velocity of the jet particles, h is the scale height – that is, the radius of the jet – and R is the radius of the jet curvature (Begelman et al. 1979).

Assuming that the groups are approximately virialised, meaning the groups are in dynamical equilibrium, we can use P_{ICM} as a proxy for P_{ram} (e.g. Garon et al. 2019). To estimate P_{ICM}, we adopted the formula from Arnaud et al. (2010), which uses simulations from Nagai et al. (2007) and observations of 33 local clusters observed by *XMM-Newton* to calculate a universal
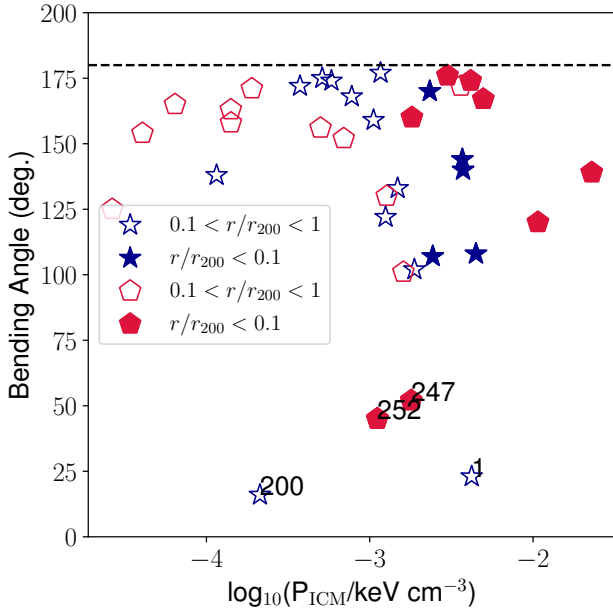
Fig. 7. P_{ICM} calculated from Eq. (3) for the X-ray galaxy group members of the COSMOS (red pentagons) and XMM-LSS (blue stars) sample as a function of the BA. The source IDs for very bent sources are annotated. The dashed line at 180° in both plots indicates a straight source.

galaxy cluster pressure profile:

$$P_{ICM}(d) = 1.65 \times 10^{-3} E(z)^{8/3} \times \left(\frac{M_{500}}{3 \times 10^{14} M_\odot} \right)^{2/3+\alpha_P+\alpha'_P(d)}$$
$$\times \, \mathbb{P}(d) \, \text{keV cm}^{-3}, \tag{3}$$

where $d = \frac{r}{r_{500}}$, $E(z) = \Omega_M(1+z)^3 + \Omega_\Lambda$, M_{500} is the group mass within r_{500}, z is the redshift and $\mathbb{P}(d)$ the generalised NFW model adopted from Nagai et al. (2007). α_P and $\alpha'_P(d)$ are fit parameters adopted from Arnaud et al. (2010). While the universal pressure profile accounts for halo mass and redshift evolution, the model from Arnaud et al. (2010) is based on local clusters assuming self-similar evolution for higher redshifts, which might not be strictly applicable to the galaxy groups we probe, though Hernández-Lang et al. (2023) show that universal pressure profiles work well up to redshifts of $z \sim 1$.

Figure 7 shows the P_{ICM} calculated from Eq. (3) for the X-ray galaxy group members of the COSMOS and XMM-LSS sample, presented in Sect. 4.2, as a function of the BA. As was expected, we find that sources in the core region ($r/r_{200} < 0.1$) are in higher pressure environments than sources of the inner region ($0.1 < r/r_{200} < 1$). For COSMOS, we do not observe a correlation between the BA and the ICM pressure. For the XMM-LSS sample, there is no correlation between BA and ICM pressure ($r_s = -0.35$, p-value = 0.16). A negative correlation between BA and pressure would be expected as it corresponds to smaller BAs at higher pressures.

We find that for group environments where $P_{ICM} \geq 10^{-3} \text{keV cm}^{-3}$, we observe a lower median BA compared to lower pressures. For $P_{ICM} \geq 10^{-3} \text{keV cm}^{-3}$, the median BAs are $BA_{med} = 139.0^{172.8}_{81.4}$ and $BA_{med} = 133.0^{163.4}_{105.0}$ for the COSMOS and XMM-LSS X-ray galaxy group members, respectively. For $P_{ICM} \leq 10^{-3} \text{keV cm}^{-3}$, the median BAs are $BA_{med} = 157.0^{164.8}_{152.2}$ and $BA_{med} = 170.0^{174.2}_{113.6}$ for COSMOS and XMM-LSS, respectively. This is consistent with the findings of Garon et al. (2019),

who estimate that P_{ram}, for which we use P_{ICM} as a proxy, has to be at least of order magnitude $10^{-3} \text{keV cm}^{-3}$ to induce jet bending. This threshold is based on an AGN triggering model from Marshall et al. (2018), who compare simulations of galaxies moving through cluster environments to observational data. For the less massive galaxy groups, such as those used in this work, the semi-analytic model of Marshall et al. (2018) predicts that, given the same velocities, galaxies must be closer to the galaxy group centre compared to galaxy clusters to be in the regime of P_{ram} induced AGN triggering. The AGN that are triggered in groups from Marshall et al. (2018) are typically found in the range $0 < r < 1r_{vir}$, with r_{vir} the virial radius of the galaxy group, which is in line with our definition of group membership up to the virial radius $1r_{200}$. Even though our limited sample size of X-ray galaxy group members does not show any significant correlation between BA and P_{ICM}, we can confirm that $P_{ICM} \sim 10^{-3} \text{keV cm}^{-3}$ works well as a threshold for ram pressure induced jet bending. We find 11 bent group members in both samples (58% in COSMOS and 65% in XMM-LSS) to be at $P_{ICM} \geq 10^{-3} \text{keV cm}^{-3}$. This includes all WATs we find in groups in COSMOS and XMM-LSS, which are expected to be predominantly bent by ram pressure (e.g. Smolčić et al. 2007; O'Dea & Baum 2023). We note an outlier, source 200 in the XMM-LSS sample, which is a NAT but is estimated to be at an ICM pressure of $2 \times 10^{-4} \text{keV cm}^{-3}$. A possible explanation for this is discussed in Appendix A, but we mention here that P_{ICM} as a proxy for P_{ram} is based on the assumption that the groups are relaxed, which might not be the case for all groups (Gozaliasl et al. 2020).

Furthermore, Marshall et al. (2018) find that higher redshift galaxy clusters ($z \sim 1$) are less constrained on the distance to the cluster centre ($0.5 \leq r/r_{vir} \leq 2$) when it comes to AGN activity triggered by ram pressure. This means that for galaxy groups at higher redshift ($z \sim 1$), sources bent due to ram pressure are found further away from the galaxy group centre compared to low redshift galaxy groups (Marshall et al. 2018). This is consistent with our results shown in the bottom panel of Figs. 4 and 5, where the bent X-ray galaxy group members show a moderate correlation between redshift and distance from the galaxy group centre (Spearman test for COSMOS sample: $r_s = 0.46$, p-value = 0.003; XMM-LSS sample: $r_s = 0.63$, p-value = 0.007). Denser cluster environments at lower redshifts fit into the accepted picture of hierarchical structure formation, shown here also for group environments.

A study by Mguda et al. (2015) looks into simulations of radio sources in cluster environments that are bent due to ram pressure. They investigate the fraction of radio galaxies that surpass the ram pressure threshold for jet bending, derived from Eq. (2) with values from Freeland & Wilcots (2011). They find that for low-mass clusters, which Mguda et al. (2015) define as $\log_{10}(M_{halo}/M_\odot) \leq 14.5$, radio sources bent due to ram pressure are most likely found within 400 kpc from the cluster centre. Bent sources in clusters with halo masses $14.0 \leq \log_{10}(M_{halo}/M_\odot) \leq 14.5$ are likely found within 800 kpc from the cluster centre.

Figure 8 shows that this relationship between group mass and projected distance from the group centre is in good agreement with the sources of our samples located in X-ray galaxy groups, where bent and very bent sources are found up to 400 kpc from the group centre in both COSMOS and XMM-LSS. The sources that are located beyond 400 kpc from the group centre are only found in halo masses $\log_{10}(M_{200}/M_\odot) \geq 13.9$. We demonstrate that the jet bending of the sources in the X-ray galaxy groups in COSMOS and XMM-LSS is well explained by ram
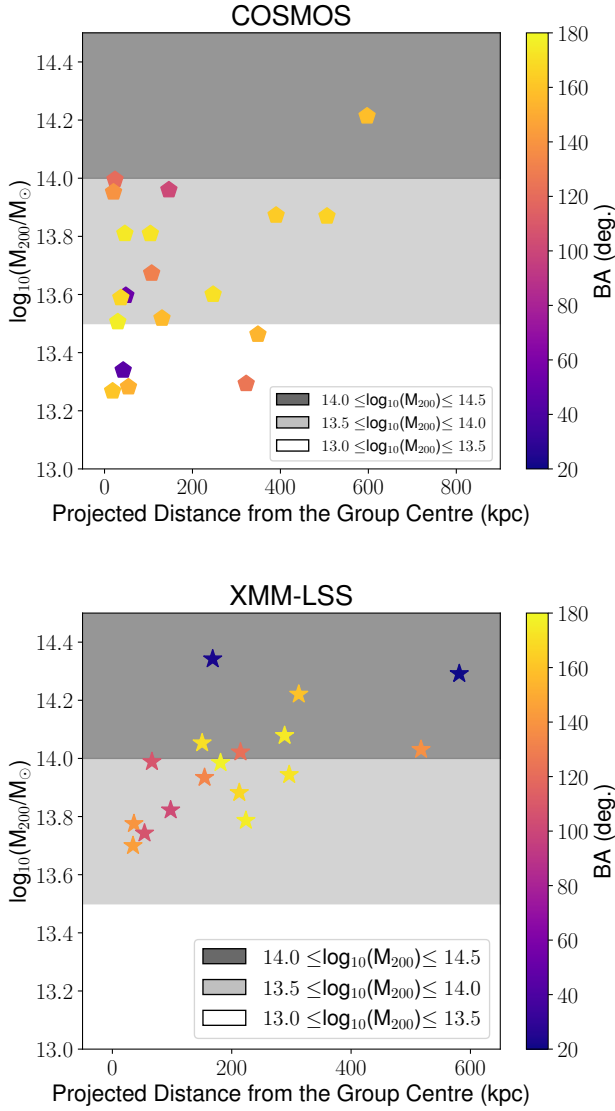
Fig. 8. Group mass, M_{200}, in $M_\odot$ as a function of projected distance from the galaxy group centre in kiloparsecs. The BAs of the sources that are found in the galaxy groups are shown by a colour scale. Top: COSMOS. Bottom: XMM-LSS.
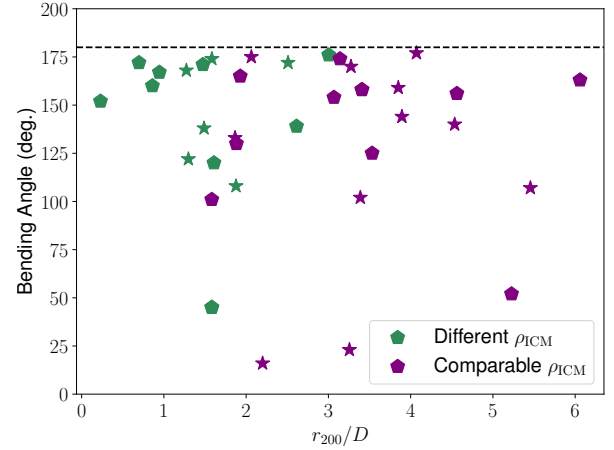

Fig. 9. Bending angle in degrees as a function of r_{200} of the galaxy groups over the radio size, D, of the bent group member in the group. The COSMOS group members are pentagons and the XMM-LSS group members are stars. If the ICM density at the end-points of the jets are within a factor of $5\rho_{ICM}$ at the host, the symbols are purple; if they are outside a factor of $5\rho_{ICM}$ at the host, they are green. The dashed line indicates a straight source.

pressure that is exerted on jets for the halo masses in the range $M_{200} = 2 \times 10^{13}\,M_\odot$ to $2.2 \times 10^{14}\,M_\odot$. The lack of correlation between halo mass and BA for group members can be due to the small sample size, as finding bent sources in galaxy groups could be rare, as is indicated by the number of WATs we find: for COSMOS X-ray galaxy group members, we have robustly identified 2 WATs with BA $\leq 100°$ (~ 0.9 WATs/deg^2) and none in the X-ray galaxy group members of XMM-LSS (where for BA $\leq 160°$ we have ~ 1.3 WATs/deg^2 in COSMOS and ~ 0.6 WATs/deg^2 in XMM-LSS in galaxy groups). Mingo et al. (2019) find ~ 0.22 WATs/deg^2 in galaxy clusters from coverage of 424 deg^2, selected from LoTSS (Shimwell et al. 2017, 2019), highlighting that large area coverage is required to create large samples of bent radio sources.

5.4. Relating jet size, ICM density, and jet power

We expect that a radio source in a large cluster will experience a more or less homogeneous ICM density between the host and the jets, as the radio source itself is small compared to the size of the cluster (e.g. Garon et al. 2019). Conversely, in small galaxy groups, where the radio size can be comparable to the group size, the ICM density could be significantly higher or lower at the jets compared to the host. To investigate this phenomenon in our sample of group members, we divide the values of P_{ICM} from Eq. (3) by the mean group temperature to obtain the expected ICM density ρ_{ICM} at the host position and the end-points of both jets for each source. We then sub-divide all group members into sources where the ICM density at the end-points of the jets is within or outside a factor of $5\rho_{ICM}$ at the host. This arbitrary threshold is chosen to generate two roughly equally sized sub-samples of sources where ρ_{ICM} is comparable at the jets and the host and where ρ_{ICM} is different between the jets and the host.

Figure 9 shows the BAs of the group members in XMM-LSS and COSMOS as a function of r_{200} of the galaxy groups over the radio size D of the bent group member. The sub-populations described above are highlighted with different colours. The sub-sample of group members where the ICM density of the jets is within a factor of $5\rho_{ICM}$ at the host is overwhelmingly found at $r_{200}/D > 3$, where the virial radius r_{200} is larger than the radio source itself and a more homogeneous ICM around the source is expected. Conversely, at $r_{200}/D < 3$ we find the population of sources where the ICM density of the jets is outside a factor of 5 from ρ_{ICM} at the host. Here, the group size and radio size are comparable and the ICM density gradient is apparent along the radio source.

While we can confirm that the ICM density varies between the jets and the host depending on how comparable the radio size is to the group size, we find no correlation with the BA. A K-S test shows that the BAs from the two populations in Fig. 9 come from the same parent distribution (K-S statistic = 0.35, p-value = 0.57). This means that the difference between the two populations is most likely driven by the jet size, as ρ_{ICM} from Eq. (3) is a function of distance from the group centre, and longer jets will therefore experience larger density gradients than shorter jets.

We combine the results regarding the intrinsic properties of our samples, namely size and luminosity, and the extrinsic
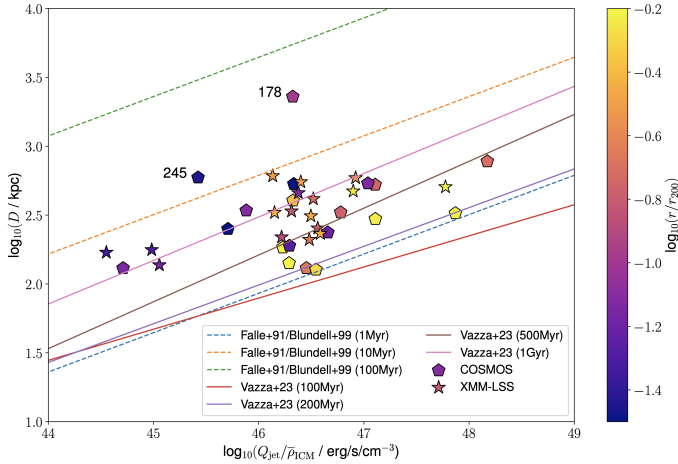
Fig. 10. Radio size, D, in kiloparsecs as a function of the jet power, Q_{jet}, over the mean ICM density, $\bar{\rho}_{ICM}$, for the group members of COSMOS (pentagons) and XMM-LSS (stars). The projected distance to the group centre in in kiloparsecs, normalised to r_{200}, is given by a colour scale. We plot dashed lines at constant t from Eq. (1) of Falle (1991), with values from Blundell & Rawlings (1999); Q_{jet} is normalised with the average $\bar{\rho}_{ICM}$ of our samples. Solid lines denote the relation between size of the radio source and jet power, normalised with the median environmental density (10^{-29} g/cm^{-3}) from the MHD simulations of Vazza et al. (2023). We note the minimum Q_{jet} value used in the simulation is 3×10^{43} erg/s, corresponding to X-axis values of 5×10^{45} erg/s/cm^{-3}, thus a simple extrapolation to lower values should be done with caution.

medium of galaxy groups, given by the ICM density. As is discussed in Sect. 5.1, Eq. (1) suggests that the size of our sources should be dependent on the jet power, the density of the surrounding medium and the lifetime of the source. We have not performed an in-depth analysis to obtain the sources' lifetimes, but we estimate the other quantities: for each group member, we estimate the jet power Q_{jet} from the radio luminosity[9] at 1.4 GHz by employing Eq. (4) from Smolčić et al. (2017a), $\log_{10}Q_{jet}(L_{1.4\,GHz}) = 0.86\log_{10}L_{1.4\,GHz} + 14.08 + 1.5\log_{10}f_W$, with $f_W \approx 4$, an uncertainty parameter. To account for the ICM density gradients our sources experience, we take the mean ICM density value $\bar{\rho}_{ICM}$ at the host and the end points of each jet, as was described above.

From Fig. 10, we can confirm that the radio size, D, increases with larger $Q_{jet}/\bar{\rho}_{ICM}$, as Eq. (1) suggests, with two notable outliers in the COSMOS sample (Source 178 and 245). $Q_{jet}/\bar{\rho}_{ICM}$ is larger for sources further away from the group centre, indicating that more powerful jets and/or a less dense medium results in larger jet sizes. A Spearman test between D and $Q_{jet}/\bar{\rho}_{ICM}$ gives a moderate correlation for the XMM-LSS group members ($r_s = 0.50$, p-value $= 0.04$). This correlation is weaker and not robust for the COSMOS group members ($r_s = 0.26$, p-value $= 0.29$). We note that the two outliers are the BGG of their group and are found in groups with halo masses $M_{200} \lesssim 10^{13.3}$ M$_\odot$, the two least massive galaxy groups that host the bent sources of our samples. Both of these sources are found at $r_{200}/D < 1$ (see Fig. 9); that is, where the radio size is larger than the virial radius of the galaxy group. For these sources, the assumption of a homogeneous ICM density around the source is not fulfilled. The sources' lifetimes are also not accounted for by our study, which could have a large impact on the jet power and size (Hardcastle et al. 2019), contributing to the scatter observed in Fig. 10. We therefore compare to models and simulations: we

use Eq. (1) from the model of Falle (1991) with characteristic values taken from Blundell & Rawlings (1999) to calculate the radio size at constant t over varying jet power (where $\rho = 2 \times 10^3$ m^{-3}, $\alpha = 1.5$, $c = 3.5$). The theoretical lines from Eq. (1) have been normalised by the median ICM density of our samples for the appropriate scaling of the X axis in Fig. 10. We also show the tracks of the average $D - Q_{jet}$ relation obtained by fitting the evolution, at 4 different epochs, of five resimulations of radio sources at the centre of a small galaxy cluster from Vazza et al. (2023), who investigated the role of a varying jet power (Q_{jet} ranging from 3×10^{43} erg/s to 1.5×10^{45} erg/s) on the overall circulation of electrons injected by the central radio galaxy. The fits from Vazza et al. (2023) have been normalised by the expected ICM density calculated from the median environmental density along the jet propagation ($\sim 10^{-29}$ g/cm^{-3}) from the MHD simulations of Vazza et al. (2023). To estimate the density of the medium the jets are expanding into, we use Eq. (2), where we take $h/R = 0.05$ as an upper limit (Begelman et al. 1979) and $(v_j/v_{gal})^2 \approx (10/3)^2$, estimated from the average galaxy velocity of our group members (see Sect. 6) and average jet velocities from Vazza et al. (2023). This gives an average ρ_{ICM} of $\approx 6 \times 10^{-3}$ cm^{-3} for the simulated sources in the centres of small clusters, which is consistent with what we find for group members in the core region of galaxy groups. We stress that Vazza et al. (2023) are simulating evolving sources and environments, where the moving ICM becomes a dominant factor after a few tens of Myr, causing the $D - Q_{jet}/\bar{\rho}_{ICM}$ lines to deviate from analytical models. After $t > 500$ Myr, the fitting formula give the average distance from the cluster centre of cosmic rays injected by jets, even if by that time they have become entirely undetectable in the radio band. While the $D - Q_{jet}/\bar{\rho}_{ICM}$ relations from Eq. (1) with values from Blundell & Rawlings (1999) are derived from broad assumptions, we are in good agreement with Pinjarkar et al. (2023), who found that the spectral ages of 28 extended radio sources in XMM-LSS (all of which are part of our XMM-LSS sample) are mostly found between 1 and 10 Myr. While we found no good agreement with the relation of Moravec et al. (2019) between radio size and distance from the group centre for the COSMOS group members (see Fig. 8), we show that, taking into account the ICM density at a given distance from the group centre, the group members of our samples grow with larger $Q_{jet}/\bar{\rho}_{ICM}$. Scatter is introduced by projection effects, the sources' lifetimes and the fact the ICM density gradients are not negligible on the scales of the jets in small galaxy groups. In Sect. 6 and Appendix A we discuss the different types of environments our sources might be interacting with. The theoretical model discussed here is most likely too simplistic to probe the diversity of these environments.

6. Estimating ICM temperature from jet bending

In the previous sections, we investigated the jet bending due to the movement of the radio AGN through the ambient medium (see Eq. (2)). We further explore this picture to include a strong magnetic field from a radio AGN that is injected into the ambient plasma by the jet, being subsequently shaped by the bulk motion of the ambient medium. New jet particles, accelerated from the central black hole, will experience a change in the direction of the magnetic field and will follow the path dictated by the magnetic field as this interacts with the surrounding medium. The BA then indicates the motion of the particles frozen to the magnetic field. Mendygral et al. (2012) used MHD simulations to show that even in a relaxed galaxy cluster, the bulk motion of the ICM significantly distorts jets and lobes injected by multiple AGN

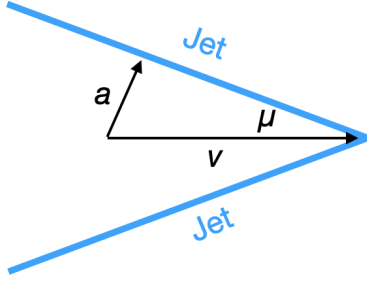[9] We assume the convention $S_\nu \propto \nu^\alpha$ for the radio spectral index.

Fig. 11. Schematic of a supersonic radio galaxy moving with velocity v through a medium with sound speed a. The Mach angle, μ, is equal to BA/2.
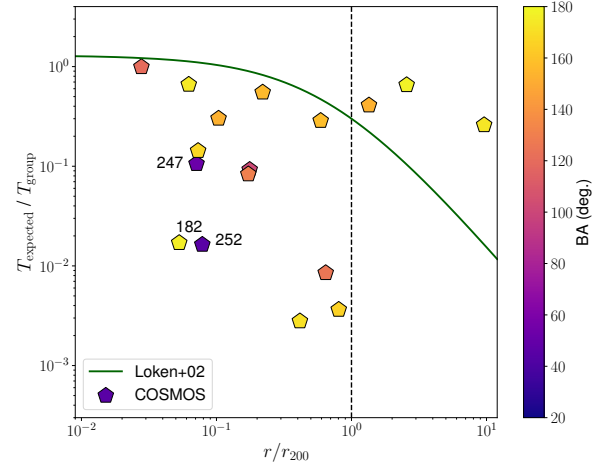

Fig. 12. Ratio of the expected temperature from Eq. (6) over the mean group temperature as a function of distance from the group centre for COSMOS sources within $10r_{200}$ and $\Delta v/\sigma_{\mathrm{disp}} < 2.7$. We show the universal galaxy cluster temperature profile of Loken et al. (2002), given by $T/T_0 = 1.3(1 + 1.5r/r_{200})^{-1.6}$. The dashed line shows the distance corresponding to the virial radius r_{200} from the group centre. The IDs of some sources are annotated. The BA of the sources is given by a colour scale.

bursts. Cosmological ENZO-MHD simulations from Vazza et al. (2021) of two radio-jet AGN inside clusters at $z = 0.5$ and $z = 1$, and the analysis of them by Vardoulaki et al. (2021b), suggest that sources at lower redshifts, which also lie in hotter and denser environments, are more bent. Additionally, these have had more opportunities for jet interaction with the IGM and a bigger volume to expand into.

We estimated the ambient temperature that is expected in order to explain the jet bending relative to a given angle, and from there we tested whether the ratio of expected temperature and the mean group temperature deviates from a typical radial profile expected for galaxy groups. We utilised the known relation between the Mach number, $\mathcal{M}$, and the angle, μ, which disturbances of supersonic flows produce with respect to the flow velocity, v:

$$sin(\mu) = \frac{1}{\mathcal{M}} = \frac{a}{v}, \quad (4)$$

where μ is the Mach angle and a is the speed of sound of a given medium (see for e.g. Springel & Farrar 2007; Massey et al. 2011, for discussion on supersonic flows). In our framework, the radio source moves with velocity v through a medium with sound speed a, where the Mach angle of the jets is then given by $\mu = \text{BA}/2$, with BA being the bending angle we assign to the source (see Fig. 11). A straight source with BA = 180° will result in a Mach number of $\mathcal{M} = 1$, whereas severely bent sources with BA = 40° will result in a Mach number of $\mathcal{M} \approx 3$. Shocks are created from the bulk motion of the medium.

From the ideal gas law, we can also estimate the temperature, T, of a given medium from the sound speed, a:

$$a = \sqrt{\frac{\gamma kT}{m}}, \quad (5)$$

where we use $\gamma = 5/3$ as the adiabatic index of the ICM, k as the Boltzmann constant, and $m = 1.66 \times 10^{-27}$ kg as the mass of ionised hydrogen. By combining Eqs. (4) and (5), we can estimate the expected temperature of the medium with which the jets of a source at a given velocity are interacting:

$$T_{\mathrm{expected}} = \frac{ma^2}{\gamma k} = \frac{mv^2}{\gamma k \mathcal{M}^2} = \frac{mv^2}{\gamma k} \times sin^2(\text{BA}/2). \quad (6)$$

To obtain the velocity values of the sources, we calculated the velocity difference for sources in the COSMOS sample, where robust spectroscopic redshifts are available within $10r_{200}$ from the group centre, given by the relative difference between the spectroscopic redshifts of the galaxy and the group, $\Delta v = \frac{|z_{\mathrm{gal}} - z_{\mathrm{group}}|}{1 + z_{\mathrm{group}}} \times c$, with c the speed of light. Due to the lack

of robust spectroscopic group redshifts, we omit the XMM-LSS group members here. To reduce the inclusion of interlopers, we restricted the sample to sources where $\Delta v/\sigma_{\mathrm{disp}} < 2.7$ (following Mamon et al. 2013), with σ_{disp} the velocity dispersion of the galaxy group that has been scaled by the radial velocity dispersion profile, adopted from More et al. (2009).

Figure 12 shows the ratio of the expected temperature from Eq. (6) over the mean group temperature as a function of distance from the group centre for COSMOS sources within $10r_{200}$ and $\Delta v/\sigma_{\mathrm{disp}} < 2.7$. Under the assumption that the jet bending is caused by the galaxy moving across the group medium, one would expect the sources to follow a typical temperature profile of groups and clusters, here shown by the universal galaxy cluster temperature profile of Loken et al. (2002), given by $T/T_0 = 1.3(1 + 1.5r/r_{200})^{-1.6}$. Compared to Loken et al. (2002), the profile we calculate for the COSMOS sources within r_{200} shows a steeper temperature gradient, while this is not seen for the three sources outside r_{200}. We cannot assign these sources securely to groups, thus we cannot rule out the possibility that their Δv, and therefore T_{expected} values are overestimated. On the other hand, the steep negative temperature gradient observed for sources within r_{200} could be evidence that the jet bending of these sources is a result of interactions with large-scale structures such as the medium of superclusters or the warm-hot intergalactic medium (WHIM), which would be at lower temperatures than the group medium. Typical temperatures for the WHIM are in the range $10^5 - 10^7$ K (see Zhao et al. 2025, and references therein). The WHIM's influence on the thermal properties of galaxy clusters is supported by both observations and simulations (see Popping & Braun 2007, and references therein), though it is one of several factors contributing to the complex temperature profiles observed in these massive structures.

As we previously mentioned, Source 252, which strongly deviates from the expected temperature profile, is part of a formation process of a large galaxy cluster, where material is accreted from the filaments of superclusters (Smolčić et al. 2007), further supporting that the media of large-scale structures can play a crucial role in shaping the jets of radio

sources, which could also explain the jet bending we observe for Source 247 (see Appendix A). Additionally, in their work on simulating radio jet distortion in cluster mergers, Domínguez-Fernández et al. (2024) discuss the creation of WAT sources as part of the early evolution of the jet and cluster merger, only forming if the burst precedes the first core passage. They note that the distortion of the radio jets is primarily influenced by bulk motions rather than the presence of substructure, and WAT-type radio AGN arise regardless of the merger's mass ratio, but depend on the jet's initial burst timing and the position of the minor cluster. In contrast, the straight Source 182 seen in Fig. 12, which is the BGG of its group, is moving slowly relative to its group ($\Delta v \approx 50 \, \mathrm{km/s}$), thus resulting in a low T_{expected} estimation from Eq. (6). Since jet bending is a complex phenomenon that is not explained by a single mechanism, this scenario will not explain all sources in our sample. However, the action of the temperature profile is evident as defining the upper limit of the BAs. Stronger bending is left unaccounted since it can be the result of the projection effects which can only reduce the observed BAs but cannot increase it.

7. Conclusions

In this work, we have investigated the bent radio sources located in the COSMOS and XMM-LSS fields, selected from visual inspection of the MIGHTEE-DR1 radio survey at $\sim$1.2–1.3 GHz with beam sizes of 8.9″ and $\sim$5″, and median central rms of $\sim$3.2–3.5 μJy/beam and $\sim$5.1–5.6 μJy/beam, respectively. We found 217 objects in XMM-LSS and 142 objects in COSMOS where we could robustly measure the BA; that is, the angle formed between the jets or lobes of a two-sided source. From these, we studied the bent radio AGN that lie within X-ray galaxy groups, 17 sources in XMM-LSS and 19 sources in COSMOS. The latter lie within groups with halo masses of $2 \times 10^{13} \lesssim M_{200c}/M_\odot \leq 3 \times 10^{14}$. We thus investigated the relations between the BA and the large-scale environment probed by the X-ray galaxy groups. We compared two methods of obtaining the BA and further compared them to studies with other methodologies and radio data of different frequencies, sensitivities, and resolution to confirm that the BA is a good method of characterising jet bending. We summarise our findings in the following:

1. There is an indication that a larger number of bent sources (BA $\leq$160°) are found at lower redshifts, in particular for objects inside X-ray galaxy groups and for halo masses $\geq 10^{13.5}\, M_\odot$, bar the small number statistics. This trend of BA with redshift persists for COSMOS and for XMM-LSS sources when we apply a halo mass cut.
   Furthermore, we find only very bent sources (BA $\leq$ 100°) at $z \leq 1$ and only straight or slightly bent sources (BA > 160°) at $z \geq 1.5$. We speculate that lower-redshift radio galaxies are statistically more bent, as they have had more time for interactions with the environment. The latter is supported by the study of Vardoulaki et al. (2021b) of MHD simulated radio sources at $z = 0.5$ and $z = 1$ using the COSMOS bent radio AGN.

2. From comparisons with simulations (Mguda et al. 2015; Marshall et al. 2018), we find that the jet bending of the sources in the X-ray galaxy groups in COSMOS and XMM-LSS can be explained by ram pressure that is exerted on jets for the halo masses in the range $M_{200} = 2 \times 10^{13}\, M_\odot$ to $2.2 \times 10^{14}\, M_\odot$. No correlation between BA and halo mass or group temperature is found for our samples, either because finding bent sources in these halo mass ranges is rare or

because interactions with superclusters play a dominant role in the jet bending.

3. We found a strong correlation between the BA and the projected distance from the X-ray galaxy group centre in the XMM-LSS field. This relation is seen in some studies in literature (Moravec et al. 2019), but not in others (Golden-Marx et al. 2021), and is also not seen in the COSMOS field, where we observe a large scatter. The relationship between BA and distance from the group centre is not straightforward. One of the parameters in play is the halo mass of the galaxy groups or clusters, but the type of IGM or ICM medium also plays an important role in jet bending.

4. We estimated the expected temperature of the medium that the jets are interacting with from the BA. For COSMOS group members, we find a steeper temperature profile than one would expect from galaxy groups, suggesting that the sources are interacting with the colder medium of superclusters or the WHIM. While the role of the WHIM in influencing jet bending is an intriguing possibility supported by environmental conditions and indirect evidence, direct observational confirmation remains elusive, warranting further investigation.

5. We found jets to be $\sim$25% less bent for sources larger than 500 kpc in X-ray galaxy groups compared to smaller sources, which is attributed to denser group environments that hinder jet expansion and promote ram pressure-induced jet bending. Less powerful sources in dense group environments are smaller compared to more powerful sources in less dense group environments. Out of 11 giant radio galaxies (2 sources in COSMOS and 9 sources in XMM-LSS) in the X-ray coverage of our samples, only 1 is found inside a group environment with a halo mass of $M_{200} \sim 2 \times 10^{13}\, M_\odot$. Incidentally, this is the largest source in the COSMOS sample.

6. The median BA for members of X-ray galaxy groups is smaller (COSMOS: $156.0^{171.1}_{117.7}$ deg; XMM-LSS: $140.0^{172.9}_{104.8}$ deg) than for objects in the field (COSMOS: $168.0^{177.0}_{140.8}$ deg; XMM-LSS: $169.0^{176.0}_{146.0}$ deg). Likewise, we find that sources located in the core region ($r/r_{200} < 0.1$) are more bent (COSMOS: $149.5^{167.4}_{128.0}$ deg; XMM-LSS: $124.0^{142.1}_{107.5}$ deg) than the sources in the inner region ($0.1 < r/r_{200} < 1$) of galaxy groups (COSMOS: $156.0^{167.4}_{128.0}$ deg; XMM-LSS: $159.0^{174.1}_{95.7}$ deg). The differences are larger for the XMM-LSS group members, either due to small-number statistics or because the COSMOS groups are selected from lower group halo masses and temperatures. Larger samples of bent sources in galaxy groups are needed for statistically robust results. We propose that the bent sources of our samples can be used as tracers for galaxy groups below the X-ray detection limit (with fluxes below $\approx 3 \times 10^{-16}\, \mathrm{erg\,s^{-1}\,cm^{-2}\,s^{-1}}$ and masses below $\approx 1.5(1 + z) \times 10^{13}\, M_\odot$ (Vardoulaki et al. 2019) or outside the X-ray coverage.

7. The very bent sources of our samples (BA $\leq$ 100°) show no intrinsic differences to the rest of our samples. In galaxy groups, we find two very bent WATs (BA < 55°) in COSMOS and two very bent NATs (BA < 25°) in XMM-LSS. The two WATs are dominant group members (the brightest and second brightest group galaxy) in groups with lower halo masses and temperatures than the two NATs, which are farther away from the group centre (infalling). This indicates that the groups of the two WATs are not relaxed and that the two NATs are moving at high velocities through the ICM.

Although the BA is a good approximation for studying the distortion of the radio structure of two-sided radio AGN, one of the

biggest limitations of the BA is the projection of radio jets on the sky, as bending from projection effects is disconnected from physical properties of the radio galaxy and its environment. One can model the projection of jets assuming the viewing angle with respect to the line of sight (e.g. Sawant et al. 2022). This can be useful for investigating individual sources but is not a feasible approach for large samples. Neural networks show promising results for deprojection tasks (e.g. Balakrishnan et al. 2019) and could be used in the future to correct the projection effects of radio jets. Nevertheless, deprojecting all sources of our samples is not trivial, and is out of the scope of this paper.

We have demonstrated the necessity of small sample studies in deep fields, with state-of-the-art multi-wavelength datasets to investigate the populations of bent radio AGN, their properties, host stellar masses, and large-scale environments. As radio astronomy is evolving and going all-sky, studies like these are crucial for training machine learning algorithms to identify bent radio AGN and investigate their relations with their large-scale environments.

Data availability

Full Tables B.1 and B.2 are only available in electronic form at the CDS via anonymous ftp to `cdsarc.cds.unistra.fr` (`130.79.128.5`) or via `https://cdsarc.cds.unistra.fr/viz-bin/cat/J/A+A/695/A178`.

References

Ahumada, R., Prieto, C. A., Almeida, A., et al. 2020, ApJS, 249, 3
Aihara, H., Arimoto, N., Armstrong, R., et al. 2018, PASJ, 70, S4
Aihara, H., AlSayyad, Y., Ando, M., et al. 2022, PASJ, 74, 247
Alam, S., Albareti, F. D., Prieto, C. A., et al. 2015, ApJS, 219, 12
Arnaud, M., Pratt, G., Piffaretti, R., et al. 2010, A&A, 517, A92
Arnouts, S., Moscardini, L., Vanzella, E., et al. 2002, MNRAS, 329, 355
Ascasibar, Y., Yepes, G., Müller, V., & Gottlöber, S. 2003, MNRAS, 346, 731
Astropy Collaboration (Robitaille, T. P., et al.) 2013, A&A, 558, A33
Balakrishnan, G., Dalca, A. V., Zhao, A., et al. 2019, Proceedings of the IEEE/CVF International Conference on Computer Vision, 171
Becker, R. H., White, R. L., & Helfand, D. J. 1995, ApJ, 450, 559
Begelman, M. C., Rees, M. J., & Blandford, R. D. 1979, Nature, 279, 770
Begelman, M. C., Blandford, R. D., & Rees, M. J. 1984, Rev. Mod. Phys., 56, 255
Best, P. N., Longair, M. S., & Rottgering, H. J. A. 1997, MNRAS, 286, 785
Bielby, R., Finoguenov, A., Tanaka, M., et al. 2010, A&A, 523, A66
Blanton, E., Gregg, M., Helfand, D., Becker, R., & White, R. 2000, ApJ, 531, 118
Blundell, K. M., & Rawlings, S. 1999, Nature, 399, 330
Borgani, S., Murante, G., Springel, V., et al. 2004, MNRAS, 348, 1078
Boyce, M. M., Hopkins, A. M., Riggi, S., et al. 2023, PASA, 40, e028
Bradshaw, E., Almaini, O., Hartley, W., et al. 2013, MNRAS, 433, 194
Brammer, G. B., van Dokkum, P. G., & Coppi, P. 2008, ApJ, 686, 1503
Capak, P., Aussel, H., Ajiki, M., et al. 2007, ApJS, 172, 99
Caproni, A., Abraham, Z., Motter, J. C., & Monteiro, H. 2017, ApJ, 851, L39
Charlton, K. K. L., Delhaize, J., Thorat, K., et al. 2025, MNRAS, 537, 272
Coil, A. L., Blanton, M. R., Burles, S. M., et al. 2011, ApJ, 741, 8
Colless, M., Peterson, B. A., Jackson, C., et al. 2003, arXiv e-prints [arXiv:astro-ph/0306581]
Condon, J. J. 1992, ARA&A, 30, 575
Cool, R. J., Moustakas, J., Blanton, M. R., et al. 2013, ApJ, 767, 118
Cooper, M. C., Aird, J. A., Coil, A. L., et al. 2011, ApJS, 193, 14
Croston, J., Hardcastle, M., Mingo, B., et al. 2019, A&A, 622, A10
Darvish Sarvestani, B. 2015, Ph.D. Thesis, University of California, Riverside, USA
Darvish, B., Mobasher, B., Martin, D. C., et al. 2017, ApJ, 837, 16
Delhaize, J., Heywood, I., Prescott, M., et al. 2021, MNRAS, 501, 3833
Dey, A., Schlegel, D. J., Lang, D., et al. 2019, AJ, 157, 168
Diemer, B. 2018, ApJS, 239, 35
Domínguez-Fernández, P., ZuHone, J., Weinberger, R., et al. 2024, ApJ, 977, 221
Drinkwater, M. J., Jurek, R. J., Blake, C., et al. 2010, MNRAS, 401, 1429
Edwards, L. O., Fadda, D., & Frayer, D. T. 2010, ApJ, 724, L143
Fabian, A. C. 2012, ARA&A, 50, 455
Falle, S. 1991, MNRAS, 250, 581
Fanaroff, B. L., & Riley, J. M. 1974, MNRAS, 167, 31P
Finoguenov, A., Guzzo, L., Hasinger, G., et al. 2007, ApJS, 172, 182
Finoguenov, A., Connelly, J., Parker, L., et al. 2009, ApJ, 704, 564
Freeland, E., & Wilcots, E. 2011, ApJ, 738, 145
Galvin, T. J., Huynh, M. T., Norris, R. P., et al. 2020, MNRAS, 497, 2730
Garilli, B., Guzzo, L., Scodeggio, M., et al. 2014, A&A, 562, A23
Garon, A. F., Rudnick, L., Wong, O. I., et al. 2019, AJ, 157, 126
Gaspari, M., Brighenti, F., D'Ercole, A., & Melioli, C. 2011, MNRAS, 415, 1549
Girardi, M., Fadda, D., Giuricin, G., et al. 1996, ApJ, 457, 61
Golden-Marx, E., Blanton, E., Paterno-Mahler, R., et al. 2019, ApJ, 887, 50
Golden-Marx, E., Blanton, E., Paterno-Mahler, R., et al. 2021, ApJ, 907, 65
Golden-Marx, E., Moravec, E., Shen, L., et al. 2023, ApJ, 956, 87
Gordon, Y. A., Boyce, M. M., O'Dea, C. P., et al. 2020, Res. Notes Am. Astron. Soc., 4, 175
Gozaliasl, G., Finoguenov, A., Khosroshahi, H., et al. 2014, A&A, 566, A140
Gozaliasl, G., Finoguenov, A., Tanaka, M., et al. 2019, MNRAS, 483, 3545
Gozaliasl, G., Finoguenov, A., Khosroshahi, H., et al. 2020, A&A, 635, A36
Gürkan, G., Hardcastle, M. J., Smith, D. J., et al. 2018, MNRAS, 475, 3010
Hale, C., Jarvis, M., Delvecchio, I., et al. 2018, MNRAS, 474, 4133
Hale, C. L., Heywood, I., Jarvis, M. J., et al. 2025, MNRAS, 536, 2187
Hardcastle, M. J., & Sakelliou, I. 2004, MNRAS, 349, 560
Hardcastle, M., Williams, W., Best, P., et al. 2019, A&A, 622, A12
Hasinger, G., Capak, P., Salvato, M., et al. 2018, ApJ, 858, 77
Hatfield, P. W., Jarvis, M. J., Adams, N., et al. 2022, MNRAS, 513, 3719
Hearin, A. P., Campbell, D., Tollerud, E., et al. 2017, AJ, 154, 190
Helfand, D. J., White, R. L., & Becker, R. H. 2015, ApJ, 801, 26
Helsdon, S. F., & Ponman, T. J. 2000, MNRAS, 315, 356

Hernández-Lang, D., Klein, M., Mohr, J. J., et al. 2023, MNRAS, 525, 24
Heywood, I., Jarvis, M., Hale, C., et al. 2022, MNRAS, 509, 2150
Hintzen, P. 1984, ApJS, 55, 533
Hunter, J. D. 2007, Comput. Sci. Eng., 9, 90
Hurley-Walker, N., Callingham, J. R., Hancock, P. J., et al. 2017, MNRAS, 464, 1146
Ider Chitham, J., Comparat, J., Finoguenov, A., et al. 2020, MNRAS, 499, 4768
Ilbert, O., Arnouts, S., Mccracken, H. J., et al. 2006, A&A, 457, 841
Ilbert, O., Capak, P., Salvato, M., et al. 2008, ApJ, 690, 1236
Ilbert, O., McCracken, H. J., Le Fèvre, O., et al. 2013, A&A, 556, A55
Jarvis, M., Taylor, R., Agudo, I., et al. 2016, in MeerKAT Science: On the Pathway to the SKA, 6
Jonas, J., & Team, M. 2016, in MeerKAT Science: On the Pathway to the SKA, 1
Jones, T., & Owen, F. 1979, ApJ, 234, 818
Jones, D. H., Read, M. A., Saunders, W., et al. 2009, MNRAS, 399, 683
Kelson, D. D., Williams, R. J., Dressler, A., et al. 2014, ApJ, 783, 110
Klein, U., Lisenfeld, U., & Verley, S. 2018, A&A, 611, A55
Kluge, M., Comparat, J., Liu, A., et al. 2024, A&A, 688, A210
Lacy, M., Baum, S., Chandler, C., et al. 2020, PASP, 132, 035001
Laigle, C., McCracken, H. J., Ilbert, O., et al. 2016, ApJS, 224, 24
Le Fèvre, O., Cassata, P., Cucciati, O., et al. 2013, A&A, 559, A14
Leauthaud, A., Finoguenov, A., Kneib, J.-P., et al. 2009, ApJ, 709, 97
Lilly, S. J., Le Brun, V., Maier, C., et al. 2009, ApJS, 184, 218
Liske, J., Baldry, I. K., Driver, S. P., et al. 2015, MNRAS, 452, 2087
Loken, C., Norman, M. L., Nelson, E., et al. 2002, ApJ, 579, 571
Lubin, L. M., & Bahcall, N. A. 1993, ApJ, 415, L17
Magliocchetti, M. 2022, A&ARv, 30, 6
Mahatma, V., Basu, A., Hardcastle, M., Morabito, L., & van Weeren, R. 2023, MNRAS, 520, 4427
Malarecki, J. M., Jones, D. H., Saripalli, L., Staveley-Smith, L., & Subrahmanyan, R. 2015, MNRAS, 449, 955
Mamon, G. A., Biviano, A., & Boué, G. 2013, MNRAS, 429, 3079
Marshall, M. A., Shabala, S. S., Krause, M. G., et al. 2018, MNRAS, 474, 3615
Massey, R., Kitching, T., & Nagai, D. 2011, MNRAS, 413, 1709
Masters, D. C., Stern, D. K., Cohen, J. G., et al. 2017, ApJ, 841, 111
Masters, D. C., Stern, D. K., Cohen, J. G., et al. 2019, ApJ, 877, 81
McLure, R., Pearce, H., Dunlop, J., et al. 2013, MNRAS, 428, 1088
McMullin, J. P., Waters, B., Schiebel, D., Young, W., & Golap, K. 2007, in Astronomical data analysis software and systems XVI, 376, 127
Mendygral, P., Jones, T., & Dolag, K. 2012, ApJ, 750, 166
Mguda, Z., Faltenbacher, A., Heyden, K. v. d., et al. 2015, MNRAS, 446, 3310
Miley, G. 1980, ARA&A, 18, 165
Mingo, B., Croston, J., Hardcastle, M., et al. 2019, MNRAS, 488, 2701
Mohan, N., & Rafferty, D. 2015, Astrophysics Source Code Library [record ascl:1502.007]
Momcheva, I. G., Brammer, G. B., Van Dokkum, P. G., et al. 2016, ApJS, 225, 27
Moravec, E., Gonzalez, A. H., Stern, D., et al. 2019, ApJ, 871, 186
Moravec, E., Gonzalez, A. H., Stern, D., et al. 2020, ApJ, 888, 74
More, S., Van Den Bosch, F. C., & Cacciato, M. 2009, MNRAS, 392, 917
Morris, M. E., Wilcots, E., Hooper, E., & Heinz, S. 2022, AJ, 163, 280
Muzzin, A., Marchesini, D., Stefanon, M., et al. 2013, ApJS, 206, 8
Nagai, D., Kravtsov, A. V., & Vikhlinin, A. 2007, ApJ, 668, 1
Navarro, J. F. 1996, in Symposium-international astronomical union (Cambridge University Press), 171, 255
Navarro, J. F., Frenk, C. S., & White, S. D. 1995, MNRAS, 275, 720
Navarro, J. F., Frenk, C. S., & White, S. D. 1997, ApJ, 490, 493
Neronov, A., Vazza, F., Brandenburg, A., & Caprini, C. 2024, arXiv e-prints [arXiv:2411.01640]
Newman, J. A., Cooper, M. C., Davis, M., et al. 2013, ApJS, 208, 5
Nishizawa, A. J., Hsieh, B. C., Tanaka, M., & Takata, T. 2020, arXiv e-prints [arXiv:2003.01511]
O'Dea, C. P., & Baum, S. A. 2023, Galaxies, 11, 67
O'Dea, C. P., & Owen, F. 1985, AJ, 90, 954
O'Donoghue, A. A., Eilek, J. A., & Owen, F. N. 1993, ApJ, 408, 428
Owen, F. N., & Rudnick, L. 1976, ApJ, 205, L1
Padovani, P., Alexander, D. M., Assef, R. J., et al. 2017, A&ARv, 25, 2
Pentericci, L., McLure, R., Garilli, B., et al. 2018, A&A, 616, A174
Pérez, F., & Granger, B. E. 2007, Comput. Sci. Eng., 9, 21
Perley, R., Willis, A., & Scott, J. 1979, Nature, 281, 437
Pinjarkar, S., Hardcastle, M. J., Harwood, J. J., et al. 2023, MNRAS, 523, 620
Polsterer, K. L., Gieseke, F., & Doser, B. 2019, Astrophysics Source Code Library [record ascl:1910.001]
Ponman, T. J., Cannon, D. B., & Navarro, J. F. 1999, Nature, 397, 135
Popping, A., & Braun, R. 2007, New Astron. Rev., 51, 24
Prestage, R. M., & Peacock, J. A. 1988, MNRAS, 230, 131

Rykoff, E., Rozo, E., Busha, M., et al. 2014, ApJ, 785, 104
Sakelliou, I., Merrifield, M., & McHardy, I. 1996, MNRAS, 283, 673
Sanderson, A. J., Ponman, T., Finoguenov, A., Lloyd-Davies, E., & Markevitch, M. 2003, MNRAS, 340, 989
Saro, A., Mohr, J. J., Bazin, G., & Dolag, K. 2013, ApJ, 772, 47
Sawant, S. M., Kosak, K., Li, K., et al. 2022, Astron. Comput., 41, 100653
Schinnerer, E., Smolčić, V., Carilli, C. L., et al. 2007, ApJS, 172, 46
Schinnerer, E., Sargent, M., Bondi, M., et al. 2010, ApJS, 188, 384
Scoville, N., Arnouts, S., Aussel, H., et al. 2013, ApJS, 206, 3
Sejake, P. K., White, S. V., Heywood, I., et al. 2023, MNRAS, 518, 4290
Shimwell, T., Röttgering, H., Best, P. N., et al. 2017, A&A, 598, A104
Shimwell, T., Tasse, C., Hardcastle, M., et al. 2019, A&A, 622, A1
Shimwell, T. W., Hardcastle, M. J., Tasse, C., et al. 2022, A&A, 659, A1
Silverman, J. D., Kashino, D., Sanders, D., et al. 2015, ApJS, 220, 12
Silverstein, E. M., Anderson, M. E., & Bregman, J. N. 2017, AJ, 155, 14
Skelton, R. E., Whitaker, K. E., Momcheva, I. G., et al. 2014, ApJS, 214, 24
Smolčić, V., Schinnerer, E., Finoguenov, A., et al. 2007, ApJS, 172, 295
Smolčić, V., Finoguenov, A., Zamorani, G., et al. 2011, MNRAS, 416, L31
Smolčić, V., Novak, M., Delvecchio, I., et al. 2017a, A&A, 602, A6
Smolčić, V., Novak, M., Bondi, M., et al. 2017b, A&A, 602, A1
Smolčić, V., Intema, H., Šlaus, B., et al. 2018, A&A, 620, A14
Springel, V., & Farrar, G. R. 2007, MNRAS, 380, 911
Straatman, C. M., van der Wel, A., Bezanson, R., et al. 2018, ApJS, 239, 27
Sweijen, F., van Weeren, R. J., Röttgering, H. J. A., et al. 2022, Nat. Astron., 6, 350
Tasse, C., Röttgering, H., Best, P., et al. 2007, A&A, 471, 1105
Taylor, M. 2011, Astrophysics Source Code Library [record ascl:1101.010]
Taylor, G., Perley, R., Inoue, M., et al. 1990, ApJ, 360, 41
Turner, R. J., & Shabala, S. S. 2015, ApJ, 806, 59
Vardoulaki, E., Andrade, E. J., Karim, A., et al. 2019, A&A, 627, A142
Vardoulaki, E., Andrade, E. J., Delvecchio, I., et al. 2021a, A&A, 648, A102
Vardoulaki, E., Vazza, F., Jiménez-Andrade, E. F., et al. 2021b, Galaxies, 9, 93
Vardoulaki, E., Gozaliasl, G., Finoguenov, A., Novak, M., & Khosroshahi, H. G. 2023, BAAS, 55, 433.08
Vazza, F., Wittor, D., Brunetti, G., & Brüggen, M. 2021, A&A, 653, A23
Vazza, F., Wittor, D., Di Federico, L., et al. 2023, A&A, 669, A50
Virtanen, P., Gommers, R., Oliphant, T. E., et al. 2020, Nat. Methods, 17, 261
Weaver, J. R., Kauffmann, O., Ilbert, O., et al. 2022, ApJS, 258, 11
Wetzel, A. R., Tinker, J. L., Conroy, C., & van den Bosch, F. C. 2014, MNRAS, 439, 2687
White, S. V., Jarvis, M. J., Häußler, B., & Maddox, N. 2015, MNRAS, 448, 2665
White, S. V., Jarvis, M. J., Kalfountzou, E., et al. 2017, MNRAS, 468, 217
White, S. V., Franzen, T. M., Riseley, C. J., et al. 2020a, PASA, 37, e018
White, S. V., Franzen, T. M., Riseley, C. J., et al. 2020b, PASA, 37, e017
Whittam, I., Jarvis, M., Hale, C., et al. 2022, MNRAS, 516, 245
Wing, J. D., & Blanton, E. L. 2011, AJ, 141, 88
Wright, E. L., Eisenhardt, P. R., Mainzer, A. K., et al. 2010, AJ, 140, 1868
Zhao, Y., Xu, H., Liu, A., et al. 2025, A&A, 695, A15

[1] IAASARS, National Observatory Athens, Lofos Nymfon, 11852 Athens, Greece
[2] Thüringer Landessternwarte, Sternwarte 5, 07778 Tautenburg, Germany
[3] Department of Physics, University of Helsinki, P.O. Box 64, FI-00014 Helsinki, Finland
[4] Dipartimento di Fisica e Astronomia, Universita di Bologna, Via Gobetti 93/2, 40122 Bologna, Italy
[5] Hamburger Sternwarte, Gojenbergsweg 112, 21029 Hamburg, Germany
[6] Istituto di Radioastronomia, INAF, Via Gobetti 101, 40122 Bologna, Italy
[7] Max-Planck-Institut für extraterrestrische Physik, Giessenbachstrasse 1, 85748 Garching, Germany
[8] Department of Computer Science, Aalto University, PO Box 15400, Espoo FI-00100, Finland
[9] Astrophysics, University of Oxford, Denys Wilkinson Building, Keble Road, Oxford OX1 3RH, UK
[10] Cosmic Dawn Center (DAWN), Copenhagen N, Denmark
[11] Niels Bohr Institute, University of Copenhagen, Jagtvej 128, 2200 Copenhagen N, Denmark
[12] Department of Astronomy, University of Massachusetts, Amherst, MA 01003, USA
[13] Space Telescope Science Institute, 3700 San Martin Dr, Baltimore, MD 21218, USA

[14] The Inter-University Institute for Data Intensive Astronomy, Department of Astronomy, University of Cape Town, Private Bag X3, Rondebosch 7701, South Africa

[15] School of Science, Western Sydney University, Locked Bag 1797, Penrith, NSW 2751, Australia

[16] CSIRO Astronomy and Space Science, PO Box 1130, Bentley, WA 6102, Australia

[17] Department of Astronomy, University of Cape Town, Private Bag X3, Rondebosch 7701, South Africa

[18] South African Radio Astronomy Observatory, 2 Fir Street, Observatory 7925, South Africa

[19] Department of Physics and Electronics, Rhodes University, PO Box 94, Grahamstown 6140, South Africa

[20] Department of Physics and Astronomy, University of the Western Cape, Robert Sobukwe Road, Bellville 7535, South Africa

[21] National Radio Astronomy Observatory, 1003 Lopezville Road, Socorro, NM 87801, USA

[22] Centre for Astrophysics Research, University of Hertfordshire, College Lane, Hatfield AL10 9AB, UK

[23] ASTRON, the Netherlands Institute for Radio Astronomy, Oude Hoogeveensedijk 4, 7991 PD Dwingeloo, The Netherlands

[24] Leiden Observatory, Leiden University, PO Box 9513, 2300 RA Leiden, The Netherlands

[25] Purple Mountain Observatory, Chinese Academy of Sciences, 10 Yuanhua Road, Qixia District, Nanjing 210023, PR China

[26] Inter-University Institute for Data Intensive Astronomy, and Department of Physics and Astronomy, University of the Western Cape, Robert Sobukwe Road, 7535 Bellville, Cape Town, South Africa

[27] School of Astronomy, Institute for Research in Fundamental Sciences (IPM), PO Box 19395-5531, Tehran, Iran

[28] Max-Planck-Institut für Astronomie, Königstuhl 17, D-69117 Heidelberg, Germany

[29] Max-Planck Institut für Radioastronomie, Auf dem Hügel 69, D-53121 Bonn, Germany

[30] South African Astronomical Observatory, PO Box 9, Observatory 7935, South Africa

[31] Department of Physics, University of Antananarivo, PO Box 906, Antananarivo 101, Madagascar

Table A.1. Properties of the very bent sources located in X-ray galaxy groups.

Source	BA (deg.)	$\log_{10}(M_{200}/M_\odot)$	kT (keV)	r/r_{200}	P_{ICM} (keV cm^{-3})
XMM-LSS Source 1	23	14.34	2.95	0.15	4.21×10^{-3}
XMM-LSS Source 200	16	14.29	2.77	0.56	2.13×10^{-4}
COSMOS Source 247	52	13.6	0.9	0.07	1.79×10^{-3}
COSMOS Source 252	45	13.34	0.66	0.08	1.11×10^{-3}

Appendix A: Very Bent Sources

A.1. Very bent sources in X-ray galaxy groups

In Table A.1, we compare the X-ray galaxy group properties for the four very bent sources discussed above. We find that the two NATs in XMM-LSS are in different X-ray galaxy group environments compared to the two WATs in COSMOS: While the two NATs in XMM-LSS are located in more massive groups ($M_{200} \approx 10^{14.3}M_\odot$) at higher temperatures ($kT \approx 2.8\,\mathrm{keV}$) and are part of the inner region of groups ($0.1 < r/r_{200} < 1$), the two WATs in COSMOS are found in less massive groups ($M_{200} \approx 10^{13.5}M_\odot$) at lower temperatures ($kT < 1\,\mathrm{keV}$) and are in the core region of their groups ($r/r_{200} < 0.1$). As we mentioned in Sect. 5, the X-ray galaxy groups in the COSMOS probe lower halo masses and group temperatures compared to XMM-LSS. This most likely plays a role in the question of why we do not observe sources with group properties like Source 1 and Source 200 from the XMM-LSS sample in COSMOS. Figure 2 shows that the very bent sources in groups are at the lower end of the group temperatures and halo masses for the bent sources in COSMOS groups, where there is little to no overlap to mass and temperature ranges of the XMM-LSS groups. In other words, the WATs in COSMOS and the NATs in XMM-LSS probe different parameter space and the reasons for the bent jets could differ, whereas in the NATs the rapid infall can be the cause of severe bending of the jets.

This may explain why we find different group environments for the very bent sources between the COSMOS and XMM-LSS sample, but not why we find very bent sources under such different environmental conditions. Under the assumption that the bending for the two NATs in XMM-LSS is driven by the ram pressure exerted on the jets as the galaxy moves through the ICM (O'Dea & Owen 1985), the environments we find for Source 1 and Source 200 from the XMM-LSS sample are well suited to explain the bending, since high temperatures statistically correspond higher velocities of the galaxies that move through the ICM (Girardi et al. 1996). Out of the four very bent sources in our samples in galaxy groups, Source 200 in XMM-LSS is the furthest away from the X-ray group centre ($r/r_{200} = 0.56$, $\sim$ 600 kpc). To induce the jet bending the ICM pressure should be higher, which would indicate that the source could be closer to the centre than calculated here. But if one assumes a flattening of the gas density (e.g. Ponman et al. 1999) and thus of the ICM profile, in the mass range we are probing, this would not play a significant role. Since the ram pressure exerted on a galaxy by the ICM scales with the square of the galaxy's velocity and only linearly with the ICM density ($P_{ram} = \rho_{ICM}\,v_{gal}^2$), this could explain the observed bending. This further supports the NAT classification of Source 200, as NATs are typically moving with high velocities through the ICM and are found at larger distances from the core region of groups and clusters (Owen & Rudnick 1976).

The two very bent sources in COSMOS are WATs, which are also believed to be predominantly shaped by ram pressure we observe for NATs (e.g. Smolčić et al. 2007; O'Dea & Baum 2023). WATs are usually found near the group or cluster centre (Hardcastle & Sakelliou 2004), as they tend to be the dominant galaxy of the group. This is consistent with our results for distance to the group centre, as is seen in Table A.1. One would expect WATs not to be located in cool cores of galaxy groups (O'Donoghue et al. 1993), but the low group temperatures we observe for Source 247 and Source 252 are not necessarily indicative of the group's core temperature, because we only have access to the mean group temperatures obtained from scaling relations. Indeed, more disturbed AGN are found in cool cores (O'Dea & Baum 2023). Smolčić et al. (2007) found that Source 252 is located in a merging group environment, where the velocities needed to explain the observed bending due to ram pressure (and buoyancy forces, dominating at the jet-tail transition) are induced by the merging event of three galaxy groups that will result in a massive galaxy cluster. In such a dynamical scenario, the measured temperature of the group environment does not reflect the final state after the merger, while the velocities already do. While Smolčić et al. (2007) give concrete evidence for this scenario for Source 252, we do not find merger candidates for Source 247 from the galaxy groups in COSMOS. Since this group is located near the edge of the X-ray coverage in COSMOS, it could be possible that Source 247 is also part of a group merger event not probed by the current X-ray data coverage. In the following section we estimate the expected temperature one would expect from the jet bending as opposed to the mean group temperature we looked at so far.

Appendix B: Sample properties

In Tables B.1 and B.2, we present the properties of the bent AGN within X-ray galaxy groups in the XMM-LSS and the COSMOS fields, respectively. These include the radio and host galaxy coordinates, redshift (spectroscopic of photometric), the largest angular size and the linear project size, the BA, flux density and radio luminosity at 1.4 GHz, as well as classification tags based on their radio structure.

Table B.1. Properties of bent AGN in XMM-LSS within X-ray galaxy groups.

Object ID	Radio RA	Radio DEC	Host RA	Host DEC	Redshift z	Redshift z_{l68}	Redshift z_{u68}	z_{ref}	LAS	Size	BA_{flux}	BA_{edge}	Flux	$\log_{10}(L_{1.4GHz})$	Tags
	(deg., J2000)		(deg., J2000)						(")	(kpc)	(deg.)	(deg.)	(mJy)	(W/Hz)	
(1)	(2)	(3)	(4)	(5)	(6)	(7)	(8)	(9)	(10)	(11)	(12)	(13)	(14)	(15)	(16)
1	33.88255	-4.68081	33.88022	-4.68296	0.348^S	-	-	PRIMUS-DR1	68	337	67	23	14.6	24.71	Jets?, NAT?
5	34.98366	-5.46760	34.98318	-5.46831	0.278^S	-	-	SDSS-DR13	108	458	163	108	53.432	25.05	Jets, bent, S-shaped
12	36.11746	-4.83127	36.11798	-4.8309	0.494^S	-	-	VIPERS	41	254	170	170	13.192	25.01	Jets, not-bent
32	34.60201	-5.41025	34.59796	-5.41684	0.648^S	-	-	PRIMUS-DR1	85	589	121	122	11.248	25.21	Jets, bent, WAT
35	34.94020	-4.89374	34.93856	-4.89252	0.333^S	-	-	SDSS-DR15	45	218	76	102	13.953	24.64	Jets? NAT?
49	35.77514	-4.20915	35.77554	-4.20929	0.631^S	-	-	PRIMUS-DR1	45	311	161	175	2.989	24.61	Jets, S-shaped
57	34.49016	-5.46774	34.48867	-5.46556	0.7^P	0.64	0.769	HSC-SSP-PDR2	70	506	151	138	7.016	25.09	Jets, bent
60	34.40662	-5.22500	34.40484	-5.22493	0.646^S	-	-	SDSS-DR15	33	232	-	159	3.133	24.66	Jets? one-sided?
84	37.61886	-4.61858	37.62289	-4.62078	0.292^S	-	-	SDSS-DR16	75	329	168	172	9.565	24.35	Jets, bent, blended
146	36.33764	-3.79950	36.33812	-3.79928	0.28^P	0.24	0.318	HSC-SSP-PDR2	41	176	142	144	1.935	23.62	Jets, bent, blended
161	34.87760	-4.07180	34.87757	-4.07146	0.601^S	-	-	SDSS-DR15	82	550	171	168	2.765	24.53	Jets, not-bent
176	33.73470	-3.79616	33.73487	-3.79625	0.14^S	-	-	SDSS-DR15	68	169	153	140	2.579	23.09	Jets, bent, blended
178	34.01987	-4.23261	34.01978	-4.23244	0.154^S	-	-	SDSS-DR15	228	608	160	174	25.329	24.17	Jets, bent, blended?
179	33.67119	-4.07914	33.67097	-4.07891	0.448^S	-	-	PRIMUS-DR1	72	414	133	133	16.996	25.02	Jets, bent, WAT?, blended
197	33.87294	-5.54909	33.87288	-5.54858	0.29^S	-	-	SDSS-DR15	48	209	164	177	32.385	24.88	Jets, not-bent, blended?
200	34.08918	-5.99792	34.08913	-5.99772	0.397^S	-	-	GAMA-DR3	88	471	89	16	2.191	24.01	Jets, bent, NAT
303	33.73724	-4.49900	33.73882	-4.49991	0.136^S	-	-	SDSS-DR15	56	137	118	107	8.337	23.57	Jets, bent

Notes. Column 1: The 1.28 GHz radio ID assigned to the source. Columns 2&3: Right Ascension and Declination of the radio position in degrees. Columns 4&5: Right Ascension and Declination of the host position in degrees. Column 5: Redshift of the radio source. The superscript 'S' and 'P' are assigned for spectroscopic and photometric redshifts, respectively. Columns 6&7: The lower and upper bounds of the redshift at 68% confidence level, respectively. Column 9: The survey from which the redshift value is obtained. Column 10: The largest angular size (LAS) of the radio source. Column 11: The projected linear size of the radio source, calculated from the largest angular size and the redshift. Column 12&13: The BA, measured from the peak flux positions of the jets or lobes (Column 12) and from the edges of the jets or lobes (Column 13), respectively. Column 14: Flux density of the radio source in mJy. Column 15: Radio Luminosity at 1.4 GHz in W Hz^{-1}, calculated using the median frequency at 1.28 GHz and a typical radio spectral index of $a = 0.7$. Column 16: Tags that describe the radio morphology. The assigned tags are chosen from jets/no-jets, one-sided, bent/not-bent, X/S/Z-shaped, WAT, NAT, blended, peculiar, and GRG, for sources that are at or greater than 1 Mpc in linear size. A '?' is added to the tag if the assessment of the tag is deemed uncertain. Full table available at the CDS.

Table B.2. Properties of bent AGN in COSMOS within X-ray galaxy groups (Table is available in the online version)

Object ID	Radio RA	Radio DEC	Host RA	Host DEC	z	Redshift z_{l68}	z_{u68}	z_{ref}	LAS	Size	BA$_{flux}$	BA$_{edge}$	Flux	$log_{10}(L_{1.4GHz})$	Tags
	(deg., J2000)								(")	(kpc)	(deg.)	(deg.)	(mJy)	(W/Hz)	
(1)	(2)	(3)	(4)	(5)	(6)	(7)	(8)	(9)	(10)	(11)	(12)	(13)	(14)	(15)	(16)
38	150.23038	2.49483	150.23055	2.49502	0.378^S	-	-	PRIMUS-DR1	35	183	-	154	0.442	23.27	Jets, not-bent, blended?
92	150.57515	1.93226	150.5735	1.93386	0.31^S	-	-	DEIMOS10k	31	141	-	125	0.407	23.04	Jets, bent, blended
178	149.99838	2.76914	149.99847	2.76906	0.166^S	-	-	SDSS-DR15	806	2289	150	152	31.1	24.32	Jets, bent, GRG
182	150.19832	1.98653	150.19832	1.98653	0.44^S	-	-	PRIMUS-DR1	33	189	175	176	21.0	25.1	Jets, not-bent, blended
192	149.75746	2.89340	149.75722	2.89339	0.351^S	-	-	SDSS-DR15	59	296	177	158	5.44	24.29	Jets, bent, Z-shaped
210	149.59712	2.44124	149.59711	2.44123	1.168^S	-	-	zCOSMOS	94	776	171	172	121.0	26.84	Jets, not-bent
213	150.62456	2.54032	150.62459	2.54031	0.432^S	-	-	VLT/FORS2	71	403	174	171	6.66	24.58	Jets, bent
218	150.20662	1.82325	150.20663	1.82326	0.53^S	-	-	SDSS-DR15	52	330	113	130	12.4	25.05	Jets, bent, S-shaped
220	149.50874	2.26135	149.50874	2.26138	0.943^S	-	-	IMACS	31	250	142	139	2.5	24.94	Jet, one-sided, blended
221	150.11786	2.68427	150.11782	2.68428	0.348^S	-	-	PRIMUS-DR1	106	525	114	101	76.9	25.43	Jets, bent, blended
225	149.60008	2.82116	149.60008	2.82116	0.345^S	-	-	SDSS-DR15	108	531	164	120	57.4	25.29	Jets, bent, S-shaped, blended
238	150.17995	1.76885	150.17999	1.76884	0.346^S	-	-	SDSS-DR9	48	236	175	174	89.2	25.49	Jets, bent, peculiar
241	150.11766	1.58572	150.11763	1.58571	0.84^S	-	-	DEIMOS10k	70	537	174	167	27.7	25.87	Jets, bent
245	150.09076	1.99999	150.09076	2.0	0.219^S	-	-	SDSS-DR15	167	592	157	160	4.84	23.78	Jets, bent, WAT?
247	149.95424	2.92122	149.95422	2.92122	0.126^S	-	-	SDSS-DR15	57	130	46	52	2.83	23.03	Jets, bent, NAT
250	150.07710	2.54897	150.07709	2.54894	0.889^S	-	-	zCOSMOS	42	326	167	165	2.8	24.93	Jets, not-bent, blended
252	150.11432	2.35647	150.11434	2.35647	0.22^P	0.348	-	3D-HST	96	341	73	45	12.0	24.18	Jets, bent, WAT
257	150.27806	1.55567	150.27807	1.55558	0.358^P	-	0.373	COSMOS2020	25	127	170	163	2.4	23.95	Jets, not-bent
258	149.94295	2.60061	149.94297	2.60063	0.344^S	-	-	zCOSMOS	26	130	-	156	18.6	24.8	Jets, not-bent, blended?

Notes. Column 1: The 1.28 GHz radio ID assigned to the source. Columns 2&3: Right Ascension and Declination of the radio position in degrees. Columns 4&5: Right Ascension and Declination of the host position in degrees. Column 5: Redshift of the radio source. The superscript 'S' and 'P' are assigned for spectroscopic and photometric redshifts, respectively. Columns 6&7: The lower and upper bounds of the redshift at 68% confidence level, respectively. Column 9: The survey from which the redshift value is obtained. Column 10: The largest angular size (LAS) of the radio source. Column 11: The projected linear size of the radio source, calculated from the largest angular size and the redshift. Column 12&13: The BA, measured from the peak flux positions of the jets or lobes (Column 12) and from the edges of the jets or lobes (Column 13), respectively. Column 14: Flux density of the radio source in mJy. Column 15: Radio Luminosity at 1.4 GHz in W Hz^{-1}, calculated using the median frequency at 1.28 GHz and a typical radio spectral index of $a = 0.7$. Column 16: Tags that describe the radio morphology. The assigned tags are chosen from jets/no-jets, bent/not-bent, X/S/Z-shaped, WAT, NAT, blended, peculiar, and GRG, for sources that are at or greater than 1 Mpc in linear size. A '?' is added to the tag if the assessment of the tag is deemed uncertain. Full table available at the CDS.